REPORT DOCUMENTATION PAGE

Form Approved OMB NO. 0704-0188

1. REPORT DATE (DD-MM-YYYY) 26-11-2019	2. REPORT TYPE Final Report	3. DATES COVERED (From - To) 1-May-2016 - 30-Apr-2019

4. TITLE AND SUBTITLE
Final Report: Two-Dimensional Growth of Free-Standing Nanosheets and Heterostructures by Ionic Layer Epitaxy

5a. CONTRACT NUMBER
W911NF-16-1-0198

5b. GRANT NUMBER

5c. PROGRAM ELEMENT NUMBER
611102

6. AUTHORS

5d. PROJECT NUMBER

5e. TASK NUMBER

5f. WORK UNIT NUMBER

7. PERFORMING ORGANIZATION NAMES AND ADDRESSES
University of Wisconsin - Madison
Suite 6401
21 N Park Street
Madison, WI 53715 -1218

8. PERFORMING ORGANIZATION REPORT NUMBER

9. SPONSORING/MONITORING AGENCY NAME(S) AND ADDRESS (ES)
U.S. Army Research Office
P.O. Box 12211
Research Triangle Park, NC 27709-2211

10. SPONSOR/MONITOR'S ACRONYM(S)
ARO

11. SPONSOR/MONITOR'S REPORT NUMBER(S)
67818-MS.11

12. DISTRIBUTION AVAILIBILITY STATEMENT
Approved for public release; distribution is unlimited.

13. SUPPLEMENTARY NOTES
The views, opinions and/or findings contained in this report are those of the author(s) and should not contrued as an official Department of the Army position, policy or decision, unless so designated by other documentation.

14. ABSTRACT

15. SUBJECT TERMS

16. SECURITY CLASSIFICATION OF:			17. LIMITATION OF ABSTRACT	15. NUMBER OF PAGES	19a. NAME OF RESPONSIBLE PERSON Xudong Wang
a. REPORT UU	b. ABSTRACT UU	c. THIS PAGE UU	UU		19b. TELEPHONE NUMBER 608-890-2667

Standard Form 298 (Rev 8/98)
Prescribed by ANSI Std. Z39.18

RPPR Final Report
as of 09-Dec-2019

Agency Code:

Proposal Number: 67818MS **Agreement Number: W911NF-16-1-0198**

INVESTIGATOR(S):

Name: Xudong Wang
Email: XUDONG@ENGR.WISC.EDU
Phone Number: 6088902667
Principal: Y

Organization: **University of Wisconsin - Madison**
Address: Suite 6401, Madison, WI 537151218
Country: USA
DUNS Number: 161202122 EIN: 396006492
Report Date: 31-Jul-2019 Date Received: 26-Nov-2019
Final Report for Period Beginning 01-May-2016 and Ending 30-Apr-2019
Title: Two-Dimensional Growth of Free-Standing Nanosheets and Heterostructures by Ionic Layer Epitaxy
Begin Performance Period: 01-May-2016 **End Performance Period:** 30-Apr-2019
Report Term: 0-Other
Submitted By: Xudong Wang Email: XUDONG@ENGR.WISC.EDU
Phone: (608) 890-2667
Distribution Statement: 1-Approved for public release; distribution is unlimited.

STEM Degrees: 9 **STEM Participants:** 7

Major Goals: Task 1: Understand the kinetics that controls the thickness and monocrystalline size. Two governing factors (GFs) that control the nanosheet thickness will be studied: (1) the strength of the electric field built by the ionic surfactant monolayer; and (2) the ionic strength in the bulk phase. A relationship between the two GFs and the thicknesses of the amorphous and monocrystalline nanosheets will be established and advanced to a generic model that describes ILE and predicts the growth outcomes. Ex-situ and in-situ TEM study will be conducted to reveal how the large number of nuclei align and grow into large monocrystalline sheets, which determines the monocrystalline size.

Task 2: Explore the growth of nanosheets of other materials by ILE. Guided by the rich library of aqueous solution synthesis recipes of inorganic nanomaterials in literature, the ILE technique will be applied to the growth of free-standing ultrathin nanosheets from broader material systems, including oxides, chalcogenides, and metals. Existing recipes in literature will be integrated with ionic surfactant monolayer systems to alter the morphology of the products from these recipes producing ultrathin nanosheets.

Task 3: Growth of nanosheet heterostructures by ILE. Following the success of ILE growth of a number of materials, we will investigate the growth of nanosheet heterostructures with either side-by-side lateral junctions or face-to-face vertical junctions. Multilayer nanosheets vertical heterostructures will be synthesized by integrating ILE with liquid phase epitaxy. Lateral nanosheet homo-/heterojunctions will be synthesized by constructing two ILE systems in the same aqueous solution using a monolayer consisting of two immiscible ionic surfactants.

Accomplishments: 1. Unit Cell Level Thickness Control of Single-Crystalline Zinc Oxide Nanosheets Enabled by Electrical Double-Layer Confinement

To obtain a comprehensive understanding of the growth kinetics in the ionic layer epitaxial (ILE) growth is significant to control the thickness and monocrystalline size of two dimensional (2D) nanomaterials for this interfacial growth. In ILE, amphiphilic molecules self-assemble into a monolayer at the water-air interface, serving as a template to direct the nucleation and growth of a crystalline nanosheet underneath. The influences of surfactant monolayer packing density were systematically investigated in ILE ZnO nanosheet growth. By adjusting the surfactant spreading area at the water surface, nanometer-thick single crystalline ZnO nanosheets were synthesized with various sizes, thicknesses and densities. We demonstrated Stern layer controls the thickness of the grown films. As the surface pressure was adjusted from 3.09 mN/m to 16.40 mN/m, ZnO nanosheets with one to four unit cell thickness were achieved. Further analysis of the nanosheet size and density yielded more insights into the nanosheet growth kinetics. It suggested that nanosheet growth was dominated by the steric hindrance from the surfactant monolayer at lower surface pressure; while the nucleation density became the dominating factor at higher surface pressure. The ZnO nanosheets with reduced thickness exhibited lower work function indicating a potential to achieve tunable band alignment in semiconductor device design. This fundamental study of ZnO nanosheets growth validated a critical hypothesis of the self-limited thickness control in ILE. It further shed light on ILE growth kinetics in correlation to the surfactant packing density. This work will open up a new method to control the synthesis of novel 2D nanosheets from non-layered materials

2. Wafer-scale synthesis of ultrathin CoO nanosheets with enhanced electrochemical catalytic properties

Through the ILE growth, we reported a large-scale nanometer-thick polycrystalline CoO nanosheet fabricated by a facile ILE approach. The film size could reach wafer scale and the film thickness was only 2.8 nm. This CoO nanosheet achieved significantly higher OER catalytic performance compared with bulk CoO owing to the very large surface atom ratio and ultra-small cross-plane charge diffusion length. This is the first solution based bottom-up synthesis of nanometer-thick CoO nanosheets, which exhibited drastically enhanced catalytic properties compared to its bulk form. This work shows the promise of the ILE technique in synthesizing 2D nanomaterials from a broad range of functional oxides with unprecedented performance gains.

3. Wafer-scale 1-nm Ni(OH)2 Nanosheet with Orders of Magnitude Higher Turnover Frequency for Oxygen Evolution Reaction

We reported a wafer-scale 1.4 nm Ni(OH)2 nanosheet fabricated by ILE. The Ni(OH)2 nanosheet achieved significantly higher OER catalytic performance compared to thicker Ni(OH)2 layers owing to the very large surface atom ratio and ultra-small cross-plane charge diffusion length. At a overpotential of 300 mV, the 1.4 nm Ni(OH)2 nanosheet delivered a TOF value of 1.12 s-1, which was over 3.6 and 120 times higher than those of the 7.0 nm and 230 nm Ni(OH)2 layers, respectively. The ILE technology for synthesizing wafer-scale oxide 2D nanomaterials is exceptionally valuable for developing catalysts with unprecedented mass activity from rare and precious catalyst materials.

4. Ionic Layer Epitaxy of Nanometer-Thick Palladium Nanosheets with Enhanced Electrocatalytic Properties

By ILE, we demonstrated a successful growth of ultrathin Pd nanosheets, which employs a cationic oleylamine monolayer at the water–air interface as a soft template to guide the nanosheet growth. The Pd nanosheets exhibited a quasi-square morphology with a uniform thickness of 2 nm and sizes ranging from 1 to 6 um. Owing to the extremely large surface-to-volume ratio arisen from the ultrathin feature together with the exposure of mixed surface crystal facets including highly active (100) facets, the Pd nanosheets exhibited high activity in formic acid oxidation compared to the commercial Pd black and other reported Pd nanostructures. This work offered a simple and effective approach toward rational design and synthesis of ultrathin metallic 2D nanosheets with enhanced functionality.

5. ILE ZnO nanosheets at the water-oil interface with highly-concentrated Zn vacancies

We demonstrated 2D ferromagnetic ZnO nanosheets synthesized by ILE at the water-oil interface as a result of highly-concentrated Zn vacancies. After annealing, the nanosheets showed characteristic magnetic hysteresis loop with a saturation magnetization of 57.2 emu/g at 5 K and 50.9 emu/g at room temperature. This value is also roughly 10 times larger than other ZnO nanostructures and comparable to conventional ferrimagnetic material Fe3O4. The mechanisms identified for the origin of the high magnetism in ZnO nanosheets suggests that they could be utilized to develop a family of magnetic semiconductor oxides for 2D spintronic and other magnetic applications.

6. Bioinspired Synthesis of Quasi-Two-Dimensional Monocrystalline Oxides

Inspired by the biomineralization processes that commonly implement organic templates with both positive and negative charges for regulating the crystal nucleation and growth, we adapted mix-charges amphiphilic monolayer to the ionic layer epitaxy and enabled the growth of monocrystalline 2D oxides nanosheets. In situ grazing incidence X-ray diffraction revealed that mixing charge in the template is able to tune the 2D crystal nucleation rate and promote the growth of monocrystalline domains. Molecular dynamics simulations suggested mixing charges could yield a stable, flatter, and more ordered monolayer template with a nonuniform distribution of charges. The mix-charge template showed great promises as a versatile synthesis paradigm for creating quasi-2D nanomaterials from a wide range of oxides, beyond van der Waals solids. This new 2D nanomaterial system will lead to the emerging of new or enhanced physical properties such as ferromagnetism, superconductivity, and single-photon emission.

7. Memristive Behavior Enabled by Amorphous-Crystalline Two Dimensional Oxide Heterostructure

We demonstrated emergence of memristive behavior in amorphous-crystalline 2D oxide heterostructures, synthesized by atomic layer deposition of a few-nm amorphous Al2O3 layers onto atomically thin single crystalline ZnO nanosheets. The conduction mechanism is identified based on classic oxygen vacancy conductive channels. ZnO nanosheets provide a 2D host for oxygen vacancies, while the amorphous Al2O3 facilitates the generation and stabilization of the oxygen vacancies. From the slope of the fitting curve, the mobility at low resistance state was estimated to be ~2400 cm2V-1s-1, which is the highest value reported in semiconductor oxides. The 2D heterointerface offers opportunities for new design of high performance memristor devices.

8. Enhanced Ferromagnetism from Organic−Cerium Oxide Hybrid Ultrathin Nanosheets

We demonstrated significantly enhanced room-temperature ferromagnetism observed from ultrathin cerium oxide nanosheets hybridized with organic surfactant molecules. The hybrid nanosheets were synthesized by ILE over a large area at the water−air interface. The nanosheets exhibited a saturation magnetization of 0.149 emu/g as their thickness reduced to 0.67 nm. This value was 5 times higher than that for CeO2 thin films and more than 20 times higher than that for CeO2 nanoparticles. This work brings an effective strategy of introducing strong ferromagnetism to functional oxide materials, which leads to a promising route toward exploring new physical properties in 2D hybrid nanomaterials.

More details on these works are included in a PDF document, uploaded in the "Upload" section

Training Opportunities: Training activities:
Supported by this project, two postdoc Yizhan Wang, Peng Tian, four graduate students Xin Yin, Ziyi Zhang, Guangyuan Yan, and Corey Carlos, three undergraduate students Yanbing Wei, Kevin Jordan Berg and Karishma Bhawnani were involved in this project and got trained in experimental skills of the 2D nanosheets sample synthesis, and characterization, and proficient operations of scanning electron microscope, X-ray photoelectron spectroscope, SQUID Magnetic property measurement system, atomic force microscope and transmission electron microscope.

Professional developments:
1. Supported by this projects, graduate students Xin Yin and Ziyi Zhang attended “Raman/AFMRaman/TERS Workshop” to get trained in using Raman spectroscopy to study 2D nanosheets, at Northwestern University in September 2016.
2. Supported by this project, one graduate student Xin Yin attended the 2017 Spring Materials Research Society (MRS) meeting to present his work at Phoenix, Arizona in April 2017.
3. Postdoc Peng Tian and Yizhan Wang, graduate students Xin Yin and Ziyi Zhang, attended the “X-ray Photoelectron Spectroscopy (XPS) Workshop 2017” to get trained in using XPS to investigate 2D nanosheets, at Northwestern University in May 2017.
4. Supported by this projects, graduate students Ziyi Zhang, Corey Carlos, Guangyuan Yan and Postdoc Yizhan Wang did the grazing incidence X-ray diffraction experiments to study the growth process of nanosheets at Argonne national lab in Feb. of 2018.
5. One graduate student Ziyi Zhang attended the 2018 Gordon Research Conference of Solid State Studies in Ceramics to present the Ionic Layer Epitaxy work at South Hadley, MA.
6. Supported by this projects, graduate students Ziyi Zhang, Corey Carlos, Guangyuan Yan and undergraduate student Kevin Jordan Berg did the grazing incidence X-ray diffraction experiments to study the growth process of nanosheets at Argonne national lab in Oct. of 2018.
7. One graduate student Corey Carlos attended the 2019 MRS spring meeting to present the Ionic Layer Epitaxy work at Phoenix.

Results Dissemination: Conference:
1. The work on the investigation of the growth kinetics and the control over the crystalline size of ZnO nanosheets were presented as a poster at the 2017 Spring Materials Research Society (MRS) meeting at Phoenix, Arizona.
2. The work of ionic layer epitaxy of oxides nanosheets was presented as a poster at the 2018 Gordon Research Conference of Solid State Studies in Ceramics at South Hadley, MA.
3. The work on ionic layer epitaxy growth of two-dimensional oxides with exotic electronic properties were presented as a talk at the 2019 Spring Materials Research Society (MRS) meeting at Phoenix, Arizona.

Publicatioins (*: Corresponding author):
1. Unit Cell Level Thickness Control of Single-Crystalline Zinc Oxide Nanosheets Enabled by Electrical Double-Layer Confinement
Xin Yin, Yeqi Shi, Yanbing Wei, Yongho Joo, Padma Gopalan , Izabela Szlufarska, and Xudong Wang* Langmuir, 33, 7708, 2017
2. Wafer-scale synthesis of ultrathin CoO nanosheets with enhanced electrochemical catalytic properties
Fei Wang‡, Yanhao Yu‡, Xin Yin, Peng Tian, and Xudong Wang* (‡: Equal contribution) Journal of Materials Chemistry A, 5, 9060, 2017
3. A wafer-scale 1 nm Ni(OH)2 nanosheet with superior electrocatalytic activity for the oxygen evolution reaction
Peng Tian, Yanhao Yu, Xin Yin and Xudong Wang* Nanoscale, 10, 5054, 2018
4. Ionic Layer Epitaxy of Nanometer-Thick Palladium Nanosheets with Enhanced Electrocatalytic Properties
Xin Yin, Qinyi Chen, Peng Tian, Pei Zhang, Ziyi Zhang, Paul M. Voyles, and Xudong Wang* Chem. Mater., 30, 3308, 2018
5. Bioinspired Synthesis of Quasi-Two-Dimensional Monocrystalline Oxides
Yizhan Wang, Yeqi Shi, Ziyi Zhang, Corey Carlos, Chenyu Zhang, Karishma Bhawnani, Jun Li, Jingyu Wang, Paul M. Voyles, Izabela Szlufarska, and Xudong Wang*
Chem. Mater. 2019, 31, 21, 9040-9048
6. Massive Vacancy Concentration Yields Strong Room-Temperature Ferromagnetism in Two-Dimensional ZnO
Xin Yin, Yizhan Wang, Ryan Jacobs, Yeqi Shi, Izabela Szlufarska, Dane Morgan and Xudong Wang*
Nano Lett. 2019, 19, 10, 7085-7092
7. Enhanced Ferromagnetism from Organic–Cerium Oxide Hybrid Ultrathin Nanosheets
Guangyuan Yan, Yizhan Wang, Ziyi Zhang, Jun Li, Corey Carlos, Lazarus N. German, Chenyu Zhang, Jingyu Wang, Paul M. Voyles and Xudong Wang*
ACS Appl. Mater. Interfaces 2019, XXXX, XXX, XXX-XXX
Publication Date:November 5, 2019
https://doi.org/10.1021/acsami.9b15841
8. Memristive Behavior Enabled by Amorphous-Crystalline Two Dimensional Oxide Heterostructure
Xin Yin, Yizhan Wang, Tzu-hsuan Chang, Pei Zhang, Jun Li, Panpan Xue, Yin Long, J. Leon Shohet, Paul M. Voyles, Zhenqiang Ma, Xudong Wang*
Nature electronics (under revison)
9. Nanoparticle-Decorated Ultrathin La2O3 Nanosheets as An Efficient Electrocatalysis for Oxygen Evolution Reactions
Yan, Guangyuan; Wang, Yizhan; Zhang, Ziyi; Dong, Yutao; Wang, Jingyu; Carlos, Corey ; Zhang, Pu; Cao, Zhiqiang; Mao, Yanchao; Wang, Xudong*
Nano-Micro Letters (under revison)
10. In Vitro Study of Enhanced Photodynamic Cancer Cell Killing Effect by Nanometer-thick Gold Nanosheets
Zhang, Ziyi; Ni, Dalong; Wang, Fei; Yin, Xin; Goel, Shreya; German, Lazarus; Wang, Yizhan; Li, Jun; Cai, Weibo; Wang, Xudong *
Nano Research (under review)

Honors and Awards: PECASE Award, 2019

Protocol Activity Status:

Technology Transfer: Nothing to Report

PARTICIPANTS:

Participant Type: PD/PI
Participant: Xudong Wang

Person Months Worked: 15.00 **Funding Support:**
Project Contribution:
International Collaboration:
International Travel:
National Academy Member: N
Other Collaborators:

Participant Type: Postdoctoral (scholar, fellow or other postdoctoral position)
Participant: Yizhan Wang
Person Months Worked: 15.00 **Funding Support:**
Project Contribution:
International Collaboration:
International Travel:
National Academy Member: N
Other Collaborators:

Participant Type: Undergraduate Student
Participant: Kevin Berg
Person Months Worked: 3.00 **Funding Support:**
Project Contribution:
International Collaboration:
International Travel:
National Academy Member: N
Other Collaborators:

Participant Type: Graduate Student (research assistant)
Participant: Ziyi Zhang
Person Months Worked: 15.00 **Funding Support:**
Project Contribution:
International Collaboration:
International Travel:
National Academy Member: N
Other Collaborators:

Participant Type: Graduate Student (research assistant)
Participant: Corey Carlos
Person Months Worked: 15.00 **Funding Support:**
Project Contribution:
International Collaboration:
International Travel:
National Academy Member: N
Other Collaborators:

Participant Type: Undergraduate Student
Participant: Karishma Bhawnani
Person Months Worked: 3.00 **Funding Support:**
Project Contribution:
International Collaboration:
International Travel:
National Academy Member: N
Other Collaborators:

Participant Type: Graduate Student (research assistant)

Participant: Guangyuan Yan
Person Months Worked: 10.00 **Funding Support:**
Project Contribution:
International Collaboration:
International Travel:
National Academy Member: N
Other Collaborators:

Participant Type: Graduate Student (research assistant)
Participant: Xin Yin
Person Months Worked: 15.00 **Funding Support:**
Project Contribution:
International Collaboration:
International Travel:
National Academy Member: N
Other Collaborators:

Participant Type: Undergraduate Student
Participant: Yanbing Wei
Person Months Worked: 5.00 **Funding Support:**
Project Contribution:
International Collaboration:
International Travel:
National Academy Member: N
Other Collaborators:

Participant Type: Postdoctoral (scholar, fellow or other postdoctoral position)
Participant: Peng Tian
Person Months Worked: 10.00 **Funding Support:**
Project Contribution:
International Collaboration:
International Travel:
National Academy Member: N
Other Collaborators:

ARTICLES:

Publication Type: Journal Article Peer Reviewed: Y **Publication Status:** 1-Published
Journal: Chemistry of Materials
Publication Identifier Type: DOI Publication Identifier: 10.1021/acs.chemmater.9b03307
Volume: 31 Issue: 21 First Page #: 9040
Date Submitted: 11/20/19 12:00AM Date Published: 10/1/19 10:00AM
Publication Location:
Article Title: Bioinspired Synthesis of Quasi-Two-Dimensional Monocrystalline Oxides
Authors: Yizhan Wang, Yeqi Shi, Ziyi Zhang, Corey Carlos, Chenyu Zhang, Karishma Bhawnani, Jun Li, Jingyu
Keywords: Two-Dimensional Oxides; Ionic layer epitaxy; surfactant template
Abstract: Controllable synthesis of two-dimensional (2D) monocrystalline oxide nanomaterials beyond van der Waals solids is intriguing but very challenging. Inspired by the biomineralization processes that commonly implement organic templates with both positive and negative charges for regulating the crystal nucleation and growth, we adapted mix-charges amphiphilic monolayer to the ionic layer epitaxy and enabled the growth of monocrystalline 2D nanosheets. Molecular dynamics simulations suggested that mixing charges could yield a stable, flatter, and more ordered monolayer template with a nonuniform distribution of charges, which are favorable for the growth of monocrystalline nanosheets.Designing the mixed amphiphilic monolayers resulted in the creation of ultrathin nanosheets from various oxides including CoO, Bi2O3, MnO2, and Fe3O4 as well as doped ones, opening up an opportunity to broaden the 2D nanomaterial family to functional oxides.
Distribution Statement: 1-Approved for public release; distribution is unlimited.
Acknowledged Federal Support: **Y**

Publication Type: Journal Article Peer Reviewed: Y **Publication Status:** 1-Published
Journal: Nano Letters
Publication Identifier Type: DOI Publication Identifier: 10.1021/acs.nanolett.9b02581
Volume: 19 Issue: 10 First Page #: 7085
Date Submitted: 11/20/19 12:00AM Date Published: 9/1/19 5:00AM
Publication Location:
Article Title: Massive Vacancy Concentration Yields Strong Room-Temperature Ferromagnetism in Two-Dimensional ZnO
Authors: Xin Yin, Yizhan Wang, Ryan Jacobs, Yeqi Shi, Izabela Szlufarska, Dane Morgan, Xudong Wang
Keywords: Defect engineering, non-equilibrium, non-layered metal oxide, ferromagnetism, ionic layer epitaxy
Abstract: Two-dimensional (2D) ZnO nanosheets with highly concentrated Zn vacancies (VZn) of up to approximately 33% were synthesized by ionic layer epitaxy at the water–toluene interface. This high cation vacancy concentration is unprecedented for ZnO and may provide unique opportunities to realize exotic properties not attainable in the conventional bulk form. After annealing, the nanosheets showed characteristic magnetic hysteresis with saturation magnetization of 57.2 emu/g at 5 K and 50.9 emu/g at room temperature. This value is 1 order of magnitude higher than other ZnO nanostructures and comparable to the conventional ferrimagnetic Fe3O4. Density functional theory calculations, with the support of experimental results, suggest that a high concentration of VZn (approximately one-third of the Zn sites) can form spontaneously during synthesis when stabilized by H ions, and the formation of VZn could be further facilitated by the presence of grain boundaries. It is essential to remove the H f
Distribution Statement: 1-Approved for public release; distribution is unlimited.
Acknowledged Federal Support: **Y**

Publication Type: Journal Article Peer Reviewed: Y **Publication Status:** 1-Published
Journal: ACS Applied Materials & Interfaces
Publication Identifier Type: DOI Publication Identifier: 10.1021/acsami.9b15841
Volume: Issue: First Page #:
Date Submitted: 11/20/19 12:00AM Date Published: 11/1/19 5:00AM
Publication Location:
Article Title: Enhanced Ferromagnetism from Organic–Cerium Oxide Hybrid Ultrathin Nanosheets
Authors: Guangyuan Yan, Yizhan Wang, Ziyi Zhang, Jun Li, Corey Carlos, Lazarus N. German, Chenyu Zhang,
Keywords: ferromagnetism, organic?oxide hybrid, two-dimensional nanomaterials, ionic layer epitaxy, oxygen vacancies

Abstract: Room-temperature ferromagnetism in two-dimensional (2D) oxide materials is an intriguing phenomenon for spintronic applications. Here, we report significantly enhanced room-temperature ferromagnetism observed from ultrathin cerium oxide nanosheets hybridized with organic surfactant molecules. The hybrid nanosheets were synthesized by ionic layer epitaxy over a large area at the water?air interface. The nanosheets exhibited a saturation magnetization of 0.149 emu/g as their thickness reduced to 0.67 nm. This value was 5 times higher than that for CeO2 thin films and more than 20 times higher than that for CeO2 nanoparticles. The magnetization was attributed to the high concentration (15.5%) of oxygen vacancies stabilized by surfactant hybridization as well as electron transfer between organic and oxide layers. This work brings an effective strategy of introducing strong ferromagnetism to functional oxide materials, which leads to a promising route toward exploring new physical propertie

Distribution Statement: 1-Approved for public release; distribution is unlimited.
Acknowledged Federal Support: **Y**

DISSERTATIONS:

Publication Type: Thesis or Dissertation
Institution: UNIVERSITY OF WISCONSIN?MADISON
Date Received: 08-Sep-2018 Completion Date: 8/16/17 3:16AM
Title: Study of Growth Kinetics in One Dimensional and Two Dimensional ZnO Nanostructures
Authors: Xin Yin
Acknowledged Federal Support: **Y**

1. Unit Cell Level Thickness Control of Single-Crystalline Zinc Oxide Nanosheets Enabled by Electrical Double-Layer Confinement

To obtain a comprehensive understanding of the growth kinetics in the ionic layer epitaxial (ILE) growth is doubtlessly significant to control the thickness and monocrystalline size of two dimensional (2D) nanomaterials for this interfacial growth. In ILE, amphiphilic molecules (*e.g.*, surfactants) self-assemble into a monolayer at the water-air interface, serving as a template to direct the nucleation and growth of a crystalline nanosheet underneath. It was hypothesized that the ionized head groups of the surfactants stabilize an electrical double layer in their vicinity and that the formation of this double layer controls the growth. Guided by this hypothesis, using the ZnO nanosheet growth system, we found the correlation between the packing density of the oleylsulfate monolayer and the thickness of single-crystalline ZnO nanosheets. The enhanced charge density from more densely packed surfactants induced a wider Zn^{2+} ion concentration zone at water-air interface, which yielded thicker nanosheets. The influences of surfactant packing density to the nanosheet size and density were also investigated, generating new insights into the ILE growth kinetics. Moreover, thickness-dependent work function indicated a potential for designing heterojunctions with tunable band alignment

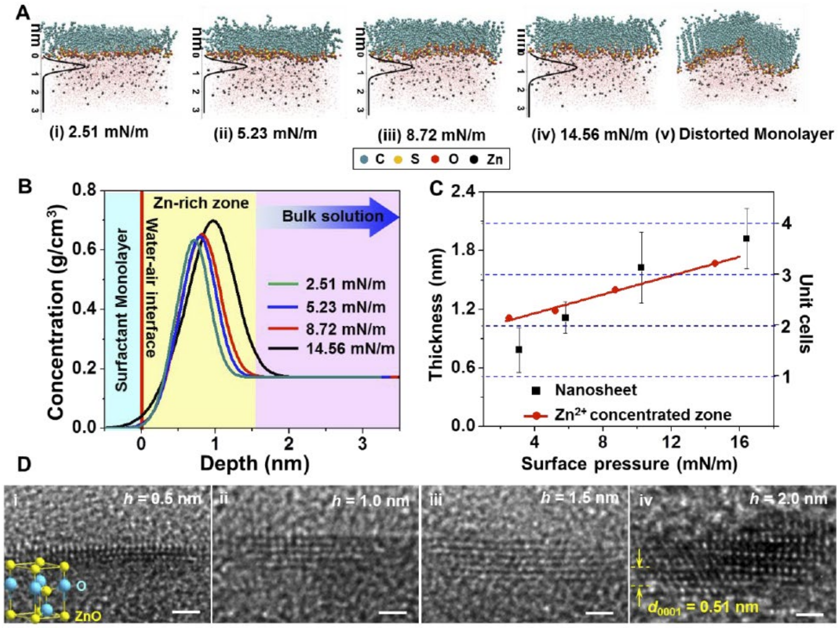

Figure 1. Influence of the surfactant monolayer packing density on the nanosheet thickness. (A) MD simulation generated Zn^{2+} ion distribution under the surfactant monolayer at different packing density. From (i) to (iv), the surface pressures are 2.51 mN/m, 5.23 mN/m, 8.72 mN/m and 14.56 mN/m, respectively. (v) represents the case with higher surface pressure where the surfactant is no longer a flat monolayer. (B) Zn^{2+} ion concentration profiles underneath the surfactant monolayer with four different surface pressures. Sky blue represents the surfactant monolayer. Light yellow represents the Zn-concentrated zone (the Stern layer). Lavender represents the bulk solution. (C) Plots of the nanosheet thickness (black squares) and the width of Zn-concentrated zone (red dots) as functions of the surface pressure. The numbers of ZnO unit cell are highlighted by dashed blue lines. (D) Cross-sectional HRTEM images of ZnO nanosheets with a thickness from one to four unit cells. Inset shows one unit cell of Wurtzite ZnO.

ZnO nanosheets were synthesized by ILE in a home-made trough reactor, where the movable crossing barrier enabled a fine control of the dispersion surface area with a resolution of 0.11 mm^2 per step. The surface pressure was measured as a function of the bar position by a

Langmuir-Blodgett trough with a Wilhelmy balance (Platinum plate) to represent the packing density of the surfactant monolayer when a 20 mL of 0.1 vol% surfactant solution in chloroform was added to the surface of the Zn precursor aqueous solution. This measurement revealed that the surfactant packing density can be continuously tuned within a relatively large range following an almost linear relation. Thus, ZnO nanosheets were synthesized *via* the standard ILE procedure at five different surface pressures (23.09 mN/m, 16.38 mN/m, 10.29 mN/m, 5.84 mN/m, and 3.09 mN/m) to investigate the surfactant packing density influences

In order to obtain a better understanding of the influence of the surfactant monolayer on the nanosheet growth at different surface pressures, MD simulations were performed to model the surfactant monolayer at the water/vacuum interface. The evolution of the oleysulfate molecules with increasing surface pressure (as controlled by the density of surfactants) is shown in Figure 1A. The range of pressures in the simulations is consistent with the pressures under which the nanosheets were experimentally achievable. The corresponding simulated distribution of Zn^{2+} resulting from the increasing electric field strengths due to packing of the surfactant monolayer is plotted in Figure 1B, where the red line represents the interface, separating the vacuum and the aqueous solution. The zinc concentration curves show a peak near the interface, right beneath the surfactant monolayer. This peak indicates the presence of a thin two-dimensional Zn-concentrated zone (less than 2 nm thick) along the interface due to the electrostatic attraction from the negatively charged monolayer.

This Zn-concentrated zone was found to evolve with the surface pressure. At low surface pressure of 3.09 mN/m, the area occupied by one molecule was large. As a result, the surfactant molecules were not uniformly ordered, as evidenced by the random packing of the carbon tails shown in Figure 1A(i). This dilute anionic surfactant packing induced a relatively weak electric field due to the low charge density. Consequently, relatively few zinc ions were attracted to the interface leading to a less concentrated and thinner zinc zone. When surface pressure was increased to 5.23 mN/m, the space between molecules became smaller and the molecules became more close-packed (Figure 1A(ii)). Thus, the charge density and therefore the electric field were both increased, resulting in a larger number of zinc ions aggregating along the interface and forming a thicker zinc-concentrated zone. Increasing the surface pressure even further (to 8.72 mN/m) resulted in a uniform ordering of the molecules (approaching the solid phase of the surfactants), an increase in the electric field was, and therefore also a thicker zinc concentrated zone (Figure 1A(iii)). Similarly, at the surface pressure of 14.56 mN/m, all the tails of the surfactant molecules were lined up along the direction perpendicular to the interface due to the smaller space between the molecules (Figure 1A(iv)). Further increase in the surface pressure led to formation of wrinkles and distorted packing (Figure 1A(v)) due to the strong repulsion between molecules (where no nanosheets could be obtained). The above results show that increasing the surface pressure (by condensing surfactant molecules) results in a transition in packing of surfactant molecules at the water/vacuum interface from random, to uniform and ordered, to distorted. The pressure regime where ZnO nanosheets can be grown experimentally corresponds to the regime where surfactants in MD simulations are ordered and form a closely packed and a relatively flat interface. MD simulations also revealed that the evolution of the morphology and density of the surfactants with pressure has a significant impact on the thickness of the Zn-concentrated region. The thickness of this region grows with increasing surface pressure (Figure 1B). We hypothesized that the thickness of the Zn-concentrated layer will affect the thickness of the experimentally grown ZnO nanosheets at corresponding pressures.

To test this hypothesis, the thicknesses of ZnO nanosheets grown at different surface pressures were measured by AFM. Multiple nanosheets (>10) were measured in each sample and their average values were plotted in Figure 1C. It can be clearly seen that as the surface pressure increased, the thickness of the as-grown nanosheets also increased monotonically. More importantly, its trend closely tracked the width of the Zn^{2+} ion concentration zone predicted by MD simulations, providing evidence for a strong correlation between the Zn^{2+} ion Stern layer and the crystalline nanosheet thickness. It should be noted that at such small thicknesses, increase of nanosheet thickness may not be continuous given the length of one ZnO unit cells is 0.52 nm along the [0001] direction. To guide the eyes, four dashed lines were added in Figure 1C to highlight the thickness of different numbers of unit cell. The average film thickness obtained from surface pressure of 5.84 mN/m and 10.29 mN/m (1.12 ± 0.16 nm and 1.63± 0.36 nm, respectively) matched well to the length of two and three unit cells. Nevertheless, the thinnest nanosheets, which were obtained at a surface pressure of 3.09 mN/m, were measured to be 0.78 ± 0.23 nm, slightly larger than one unit cell. It might be because of the relatively larger width of the Zn^{2+} ion Stern layer compared to the one unit cell thickness at this growth condition, and thus the resulted ZnO nanosheets would exhibit a combination of one and two unit cell thicknesses. As the surface pressure reached 16.38 mN/m, the nanosheet thickness rose to 1.93± 0.31 nm. This value was slightly smaller than the length of four unit cells, which might be attributed to the insufficient Zn^{2+} ion concentration to sustain the growth of four complete unit cells.

The unit cell-level thickness control was further verified by cross-sectional HRTEM images of the nanosheets (Figure 1D). Along the c-direction of Wurtzite ZnO, one unit cell has a thickness of 0.52 nm, which corresponds to three layers of bright dots (Zn ions) in the HRTEM image, *i.e.* the (0002) plane as shown in Figure 1D(i). From samples collected from higher surface pressure of 5.84 mN/m, 10.29 mN/m, and 16.38 mN/m, the number of plane (0002) increased to 5, 7 and 9, respectively, corresponding to 2, 3, and 4 unit cells as shown in Figure 1D(ii) – (iv). This analysis supports the claim that by controlling the packing density of the surfactant monolayer one can digitally tune the nanosheet thickness with a resolution of one unit cell all the way down to the thickness of one unit cell.

The influences of surfactant packing density were further investigated by statistic analysis on the nanosheet geometry over a large quantity. Statistic analysis shows that the average size started to decrease from 9.23 ± 2.55 μm^2 to 4.4 ±0.49 μm^2 as the surface pressure increased from 3.09 mN/m to 10.25 mN/m, and then increased to 21.93 ± 5.34 μm^2 when the surface pressure further rose to 16.40 mN/m. The smallest nanosheet size was obtained at 10.25 mN/m. The number of nanosheets per unit surface area, *i.e.* the nanosheet density, was also analyzed. The density dependence on the surface pressure exhibited the opposite trend than the size dependence on surface pressure.

The opposite size and density relations provide valuable insights into the ILE growth kinetics. Based on the observation of time-dependent nanosheet evolution, we previously proposed that single crystalline nanosheets were formed *via* oriented attachment of numerous nano-crystallites nucleated from the Stern layer. It follows that, the nanosheet formation is controlled by two competing factors: nucleation density and surfactant density. Higher nucleation density facilitates the attachment of discrete crystallites during the growth, which is favorable for the formation of large nanosheet. Thermodynamically, the nucleation density is directly related to the Zn^{2+} ion concentration in the Stern layer, which is proportional to the surfactant packing density. At the same time, higher surfactant packing density induces larger steric hindrance to the oriented attachment, and thus limits the formation of large nanosheet. Our experiments showed that at lower surface pressure from 3.09 mN/m to 10.25 mN/m, the steric hindrance from the surfactant monolayer dominated the nanosheet growth. That is, the higher the surfactant packing density, more resistance would be experienced during the oriented attachment of the crystallites, resulting in the decreased nanosheet size and increased nanosheet density. As the surface pressure further increased from 10.25 mN/m to 16.40 mN/m, the change of the surfactant packing density became less significant due to the already very tight space between the surfactant molecules. Nevertheless, the higher Zn^{2+} ion concentration in the Stern layer provided a much lower nucleation energy barrier to boost the nucleation density, as thus largely promoted the oriented attachment of crystallites. Therefore, much larger nanosheets with a low density were obtained in this region.

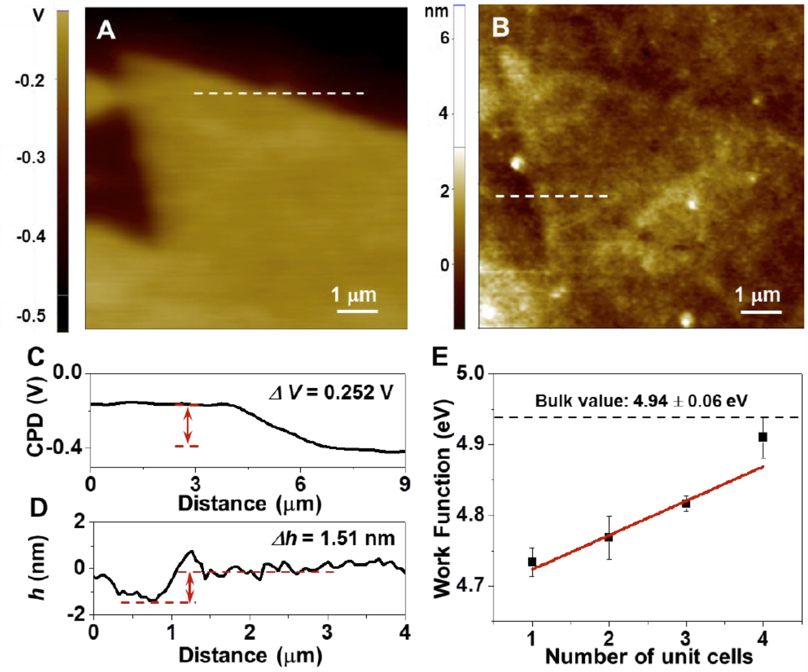

Figure 2. Work function investigation. (A) EFM image of a ZnO nanosheet rested on gold surface. (B) Corresponding AFM topographic image of the ZnO nanosheet shown in A. (C, D) Line profiles of voltage and height data extracted from A and B, respectively. (E) Work function measured by EFM as a function of nanosheet thickness. The bulk value was marked by the dashed line.

Work function is a fundamental electronic property of semiconductor materials. Here, the thickness-dependent work function was analyzed by measuring the surface potentials using scanning Kelvin probe microscopy (SKPM), where the work function was extracted from surface potential differences. The nanosheets with different thickness were supported by a Si substrate coated with a 100-nm-thick Au thin film as the reference. The surface potential mapping of one representative sample is shown in Figure 2A, revealing the uniform surface potential distribution over the entire nanosheet. The corresponding topography image is shown in Figure 2B. Along the dashed line in Figure 2A and B, the surface potential difference between ZnO nanosheet and Au thin film was measured to be 0.252 V (Figure 2C), while the nanosheet had a thickness of 1.51 nm, i.e. 3 unit cells (Figure 2D). The work function of the nanosheets was then calculated from the surface potentials following the equation ΦZnO = ΦAu - ex(CPDAu - CPDZnO), where ΦZnO is the work function of ZnO nanosheet, ΦAu is the work function of Au, which is 5.1 eV, CPDAu and CPDZnO are contact potential difference between the tip and Au film, and the ZnO nanosheet, respectively. It should be noted that while the work function of gold in the range of 4.74 eV to 5.54 eV have been reported, 5.1 eV is the often used value, particularly for flat surfaces. Thus, the work function evolution with the thickness increasing from one unit cell to four unit cells were extracted and plotted in Figure 2E, which shows increasing trend from 4.73±0.02 eV to 4.91±0.03 eV, approaching the bulk value of 4.94 ± 0.06 eV. This thickness-dependent work function provides a good flexibility in designing heterojunctions with tunable band alignment.

In summary, the influences of surfactant monolayer packing density were systematically investigated in ILE ZnO nanosheet growth. By adjusting the surfactant spreading area at the water surface, nanometer-thick single crystalline ZnO nanosheets were synthesized with various sizes, thicknesses and densities. MD simulations were performed to reveal the Zn^{2+} ion distribution profile underneath the surfactant monolayer at different packing densities (*i.e.* surface pressure). It was found that both the Zn^{2+} concentration and the width of the Zn^{2+}

concentrated zone (the Stern layer) increased monotonically with increasing surfactant packing density. Comparing experimental measurements with the simulation results revealed an excellent match between the nanosheet thickness and the Stern layer width, confirming the hypothesis that the thickness of the Stern layer controls the thickness of the grown films. As the surface pressure was adjusted from 3.09 mN/m to 16.40 mN/m, ZnO nanosheets with one to four unit cell thickness were achieved. Further analysis of the nanosheet size and density yielded more insights into the nanosheet growth kinetics. It suggested that nanosheet growth was dominated by the steric hindrance from the surfactant monolayer at lower surface pressure; while the nucleation density became the dominating factor at higher surface pressure. The ZnO nanosheets with reduced thickness exhibited lower work function indicating a potential to achieve tunable band alignment in semiconductor device design. This fundamental study of ZnO nanosheets growth validated a critical hypothesis of the self-limited thickness control in ILE. It further shed light on ILE growth kinetics in correlation to the surfactant packing density. This work will open up a new method to control the synthesis of novel 2D nanosheets from non-layered materials with thickness down on one unit cell.

2. Wafer-scale synthesis of ultrathin CoO nanosheets with enhanced electrochemical catalytic properties

With the knowledge of successful ionic layer epitaxial growth of atomic-thick single-crystalline ZnO nanosheets, we also explored the growth of nanosheets of other materials by ILE. Cobalt oxides and hydroxides are promising oxygen evolution catalysts (OER) due to appropriate binding energy between Co atom and OER species. 2D cobalt materials have shown promoted catalytic performance over their bulk counterpart. Current strategies to obtain 2D cobalt-based catalysts include hydrothermal reaction, electrodeposition and atomic layer deposition. They require harsh preparation conditions, conductive substrates, or sophisticated equipment. Producing wafer scale, continuous, and nanometer-thick cobalt oxide thin sheets is so far impractical. Through the ILE growth, we obtained large area, ultrathin CoO nanosheets grown at the water–air interface directed by oleic acid monolayers. The CoO nanosheets could be as large as the opening area of the reactor and thus enabled large-scale applications of its 2D morphology. We examined the electrochemical properties of these CoO nanosheets and discovered significant performance gain for photoelectrochemical (PEC) water splitting in comparison to their bulk form.

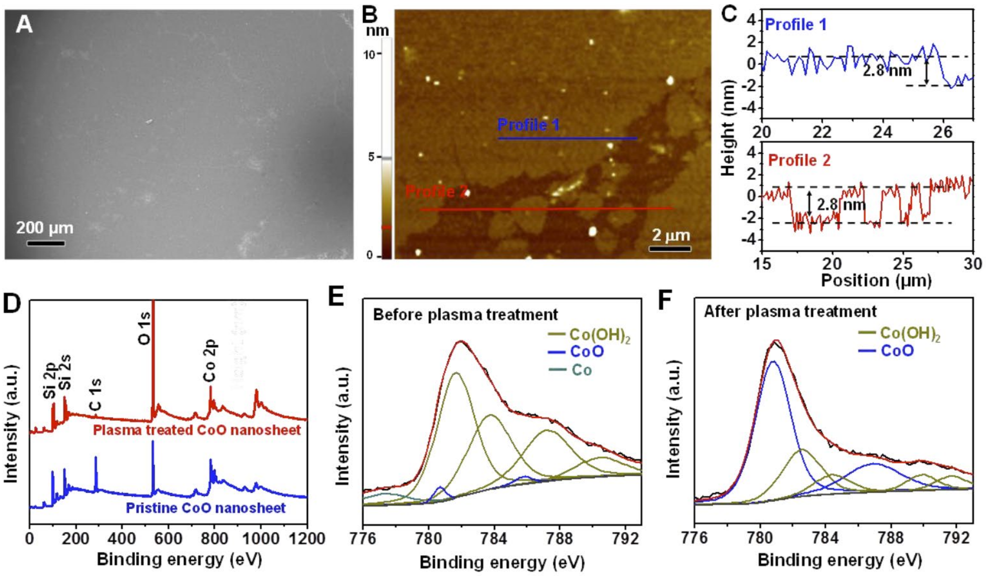

Figure 3. Characterization of CoO nanosheets. (A) SEM image of a CoO nanosheet covering a Si substrate surface. (B) AFM topography scan of a cracking area from the CoO nanosheet on a

Si wafer. (C) The height profile along the blue and red lines in (B) showing a very small roughness factor of 0.39 nm and a uniform film thickness of 2.8 nm. (D) XPS spectra of CoO nanosheets before (blue) and after (red) oxygen plasma treatment. (E) and (F) XPS of CoO nanosheets before and after O2 plasma treatment.

Figure 3A is a low magnification SEM image showing an astransferred CoO nanosheet on a Si substrate over a very large area. No obvious contrast variation could be observed because the nanosheet was continuous and uniform in thickness. There were no wrinkles or overlaps of the as-transferred nanosheet either. Sporadic brighter dots could be found on the nanosheets. They are nanoparticles picked up from the reaction solution during the transfer process. Some cracks (the slight brighter regions in the SEM image) were also observed on the nanosheets, which were likely formed during the transfer and drying. These occasional cracks offered a good observation area to determine the nanosheet thickness. The topography was scanned by using atomic force microscopy (AFM). As shown in Figure 3B, the nanosheet surface was fair smooth and flat with an average roughness factor (Ra) of only 0.39 nm, which was comparable to the reported amorphous metal oxide film. A line profile along the crack area was extracted and shown in Figure 3C, which revealed the thickness of the nanosheets was 2.8 nm. The small cracked chips inside the gap also had the same 2.8 nm thickness, further suggesting that the small pieces might come off from the nanosheet post growth, i.e. during transferring.

X-ray photoelectron spectroscopy (XPS) was employed to probe the elemental features and bonding states of this CoO nanosheet. The full XPS survey spectra clearly showed the Co, O and C peaks detected from the as-transferred pristine CoO nanosheets on a Si substrate (blue curve in Figure 3D). The C signal originated from the oleyl acid surfactant coverage. The surfactant residues could be removed by using oxygen plasma. The largely reduced C signal in plasma treated samples confirmed the successful removal of C residue after 10 minutes of oxygen plasma treatment (red curve in Figure 3d). To further reveal the chemical environment of the Co atom, the Co 2p peak of both pristine and plasma-treated CoO nanosheets was individually scanned and deconvoluted. In pristine CoO nanosheets, the majority of surface Co atoms were bonded with the OH^- group due to surfactant binding (Figure 3E). After plasma treatment, the majority peak intensity of the Co 2p spectrum could be attributed to the Co–O bonds (Figure 3F), evidencing that the bulk component of this nanosheet was CoO.

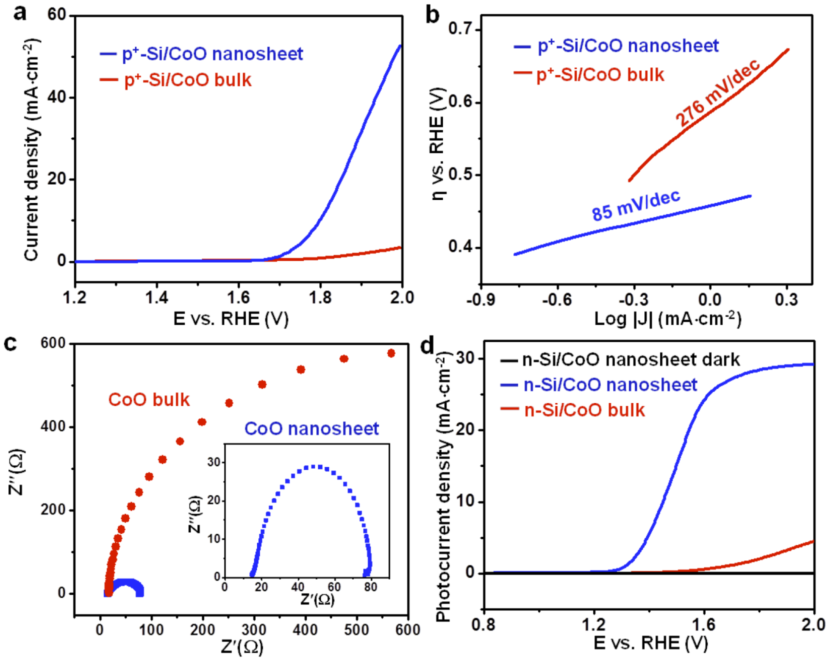

Figure 4. Electrocatalytic performance of CoO nanosheets and bulk CoO films for the OER. (A, B) Current density–potential (J–V) curves (A) and Tafel slopes (B) of CoO nanosheets and bulk

CoO films measured in 1 M NaOH aqueous solution. (C) Nyquist plots recorded at 1.9 V vs. the RHE in 1 M NaOH aqueous solution. The inset is the amplified plot of CoO nanosheets. (D) Photocurrent density–potential (Jph–V) curves of the n-Si/CoO nanosheet and n-Si/CoO bulk film measured in 1 M NaOH aqueous solution under 1 Sun illumination.

This ultrathin nanosheet possessed two advantages for catalyst applications: abundant surface active sites for binding chemicals, and the short charge diffusion length along the out-of-plane direction. To study its catalytic properties associated with its ultra-small thickness towards the OER, the CoO nanosheet was transferred onto a heavily doped p-type Si (denoted as p+-Si) substrate. As a comparison, the OER activity of CoO bulk materials was evaluated using the same p+-Si substrate. The bulk CoO film (~1 mm in thickness) was deposited on the silicon wafer using a modified thermal annealing procedure. Figure 4A illustrates the current density–potential (J–V) curves of CoO nanosheets (blue) and bulk CoO (red) measured in 1 M NaOH aqueous solution. Bulk CoO could only produce a geometric current density of 0.8 mAcm^{-2} at an overpotential (η) of 560 mV (vs. the reversible reference electrode (RHE)). At the same η of 560 mV vs. the RHE, the CoO nanosheet was able to achieve a geometric current density of 10 mA cm^{-2}, which was 12.5 times larger than that of the CoO bulk.

By extrapolating the linear region of h versus log J (Figure 4B), the Tafel slope of the bulk CoO was determined to be 276mV per decade, suggesting the slow charge transfer kinetics between bulk CoO and the electrolyte. Nevertheless, when the film thickness shrunk down to 2 nm, the Tafel slope was sharply reduced to 85 mV per decade, indicating a largely promoted interfacial kinetic compared to its bulk form. In general, the Tafel slope of the ultrathin CoO nanosheet was fairly low and only one quarter of the reported pristine CoO nanoparticles. Compared to the benchmark defective ALD CoO*x*, the CoO nanosheet could still deliver a comparable □ at a current density of 10 mA cm-2.

Similar surface kinetic variation was also revealed by the Nyquist plots obtained from electrochemical impedance spectroscopy. The recorded semicircle manifests the charge transfer resistance between the catalysis and the electrolyte interface. As shown in Figure 4C, the semicircle radius of CoO nanosheets was at least 10 times smaller than that of bulk CoO, suggesting a substantial reduction of charge transfer resistance of/across the solid/electrolyte interface. Such a significant improvement was a direct result of the nanometer film thickness as well as the largely increased surface Co atom ratio. The ultra-small film thickness ensured an efficient hole transportation with only a couple of nanometers charge diffusion length. It is also known that low-coordinated surface transitional metal cations could serve as predominate adsorption sites for electrochemical reactants (e.g., CO2 and H2O). Therefore, rapid charge transport kinetics and very high OER rates were achieved by the nanometer-thick CoO nanosheet.

The ILE-grown CoO nanosheet also offered a wafer-scale film size and continuous film structure, which greatly favored direct integration of the nanosheets with light absorbers, providing an unprecedented platform for developing binder-free photoelectrochemical (PEC) devices. These merits distinguished ILE nanosheets from other 2D nanomaterial systems that were typically micro- or nanometers in size and required additional polymer binders for large-scale catalyst manufacturing. To demonstrate this advantage, we fabricated a PEC cell by simply laying the CoO nanosheet on the surface of a n-Si wafer and measured the PEC performance with 0.1 cm2 active area in 1 M NaOH aqueous solution under one sun illumination (AM 1.5G). As shown in Figure 4D, the onset potential of the n-Si/CoO nanosheet was located at the position of 1.29 V vs. the RHE, comparable to other Si photoanodes without a buried junction. The saturated photocurrent density (Jph) reached 28.1 mA cm□2 at 1.76 V vs. the RHE, on par with that of typical planar Si photoelectrodes. The fairly low onset potential and high Jph evidenced effective coupling between the photoactive n-Si and electrochemically active CoO nanosheet under no binder conditions. On the other hand, the n-Si/bulk CoO exhibited very limited PEC performance, probably caused by the low catalytic ability and profound light blocking by the thick CoO film.

In summary, we reported a large-scale nanometer-thick polycrystalline CoO nanosheet fabricated by a facile ILE approach. The film size could reach wafer scale and thefilm thickness was only 2.8 nm. This CoO nanosheet achieved significantly higher OER catalytic performance compared with bulk CoO owing to the very large surface atom ratio and ultra-small cross-plane charge diffusion length. At a h of 560 mV vs. the RHE, the CoO nanosheet delivered a geometric current density of 10 mA cm$^{\square 2}$, which was more than one order of magnitude higher than the bulk CoO film (0.8 mA cm$^{\square 2}$ at the same $\square$). The Tafel slope of the CoO nanosheet was estimated to be 85 mA per decade, which was more than 3 times smaller than that of bulk CoO (276 mA per decade). The wafer-scale film size significantly facilitated the integration of the CoO nanosheet with a light absorbing n-type silicon wafer, enabling an efficient PEC photoanode with an onset potential of ~1.29 V vs. the RHE and a J_{ph} of 28.1 mA cm$^{\square 2}$ at 1.76 V vs. the RHE. This is the first solution-based bottom-up synthesis of nanometer-thick CoO nanosheets, which exhibited drastically enhanced catalytic properties compared to its bulk form. Although rigid Si substrates were used, ILE inherently has the compatibility with flexible devices due to the low-temperature synthesis and facile transfer process. This work shows the promise of the ILE technique in synthesizing 2D nanomaterials from a broad range of functional oxides with unprecedented performance gains.

3. Wafer-scale 1-nm Ni(OH)2 Nanosheet with Orders of Magnitude Higher Turnover Frequency for Oxygen Evolution Reaction

Besides ionic layer epitaxial growth of catalytically active CoO nanosheet, we also realized ILE growth of ultrathin $Ni(OH)_2$ nanosheet, another catalytic material for oxygen evolution reaction. We reported a development of 1.4 nm $Ni(OH)_2$ nanosheet OER catalyst over wafer scale by ionic layer epitaxy (ILE). The uniform nanometer thickness of the $Ni(OH)_2$ nanosheet across the entire wafer surface offered orders of magnitude higher mass electrochemical activity compared to typical OER catalysts. This development marks a new cornerstone for the development of efficient electrochemical catalyst.

The $Ni(OH)_2$ nanosheet was synthesized using nickel nitrate hexahydrate and hexamethylenetetramine (HMT) as precursors, and templated by a monolayer of oleic acid surfactant at the water surface. Figure 5A is a typical SEM image of an as-transferred nanosheet on a Si substrate. No obvious contrast variation could be observed because the nanosheet was continuous and uniform in thickness. Transmission electron microscopy (TEM) was then used to characterize the crystal structure of $Ni(OH)_2$ nanosheets. High-resolution TEM (HRTEM) image revealed the polycrystalline feature of the $Ni(OH)_2$ nanosheet, where individual domain was found to be ~5 nm. From the image, the (101) d-spacing was measured to be 0.235 nm. Atomic force microscopy (AFM) topography image revealed the nanosheet surface was extremely smooth and flat (Figure 5C), confirmed the thickness of the nanosheet was 1.4 nm and uniform across the entire nanosheet. X-ray photoelectron spectroscopy (XPS) was employed to probe the elemental information and bonding states of the nanosheet. The full XPS survey spectra clearly showed the Ni, O, C and Si peaks detected from the as-transferred nanosheet on a Si substrate. To further reveal the chemical state of Ni atom, the Ni 2p XPS peak of nanosheet was individually scanned and deconvoluted (Figure 5D). The peak at 855.5 eV can be attributed to Ni^{2+} in $Ni(OH)_2$, evidencing the bulk component of this nanosheet was $Ni(OH)_2$.

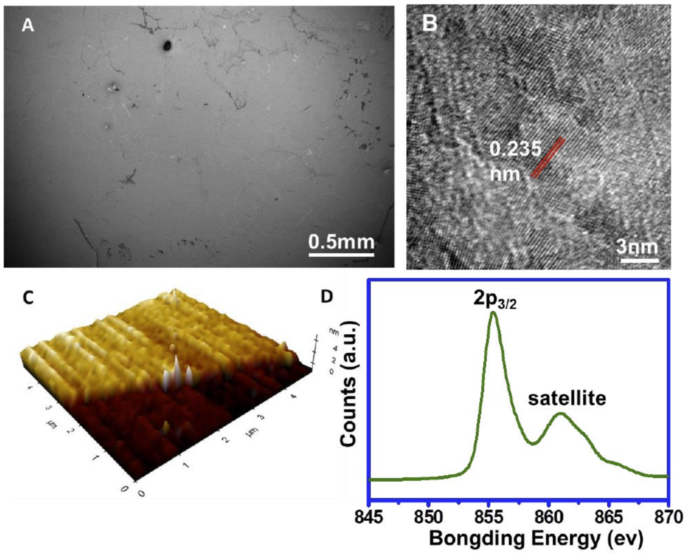

Figure 5. (A) SEM image of a $Ni(OH)_2$ nanosheet on Si substrate surface. (B) HRTEM image of the $Ni(OH)_2$ nanosheet showing its polycrystalline nature. (C) 3D AFM topography scan of a cracking area from the $Ni(OH)_2$ nanosheet. (D) High-revolution XPS of the Ni^{2+} peak.

To study catalytic behavior associated with the ultrasmall thickness towards OER, the $Ni(OH)_2$ nanosheet was transferred onto a FTO glass. As a comparison, the OER activities of thicker $Ni(OH)_2$ layers were evaluated using the same configuration. Thicker $Ni(OH)_2$ layers were prepared by either ILE or electrodeposition and their thicknesses were measured to be 7.0 nm and 230 nm. Figure 6A illustrates the current density-overpotential (j-η) curves of the 1.4 nm $Ni(OH)_2$ nanosheet measured in 1 M NaOH solution in comparison to the other two thicker films. All of them can produce a geometric current density of 10 mA/cm^2 at η = ~330 mV, which agreed well with other reported NiO_x OER catalysts. All $Ni(OH)_2$ samples displayed an oxidation peak at η from 100 mV to 200 mV. This oxidation feature is related to the oxidation of $Ni(OH)_2$ to NiOOH, and is reflective to the amount of active Ni sites. The large difference of the peak areas suggested that Ni atoms inside the bulk film were also electrochemically active.

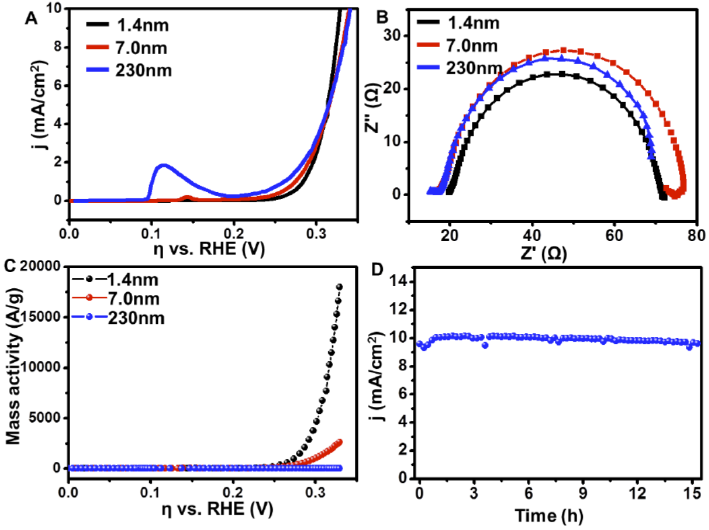

Figure 6. (A) The j-η curves measured in 1 M NaOH aqueous solution for OER. (B) Nyquist plots measured in 1 M NaOH solution at a potential of 620 mV vs. Hg/HgO. (C) Mass activity determined from j as a function of η. (D) Current density measured at η= 335mV (vs. RHE) as a function of time.

Electrochemical impedance spectroscopy was used to characterize surface kinetics of the $Ni(OH)_2$ films and the Nyquist plots were shown in Figure 6B. The semicircle in high frequency region manifests the charge transfer resistance between the catalysis and electrolyte interface. All the three samples showed a very close semicircle radius, suggesting there was no obvious variation of charge transfer resistance across the solid/electrolyte interface. Mass activity of an electrocatalyst is particularly meaningful in commercial applications. As shown in Figure 6C, a remarkable mass activity of 4662 A/g was obtained from the 1.4 nm $Ni(OH)_2$ nanosheet at η= 300 mV, approximately 3.6 and 120 times higher than that of the 7.0 nm and 230 nm $Ni(OH)_2$ layers, respectively, suggesting an extremely high exposure of active sites. Another important criterion for an OER catalyst is its operational stability. The stability of the 1.4 nm $Ni(OH)_2$ nanosheet was assessed in 1M NaOH by recording the current density as a function of time at a η= 335 mV. As shown in Figure 6D, j of the $Ni(OH)_2$ nanosheet exhibited no tendency of reduction after 15 hours of continuous oxygen evolution reaction.

To conclude, we reported a wafer-scale 1.4 nm $Ni(OH)_2$ nanosheet fabricated by ILE. The $Ni(OH)_2$ nanosheet achieved significantly higher OER catalytic performance compared to thicker $Ni(OH)_2$ layers owing to the very large surface atom ratio and ultra-small cross-plane charge diffusion length. At a η of 300 mV, the 1.4 nm $Ni(OH)_2$ nanosheet delivered a TOF value of 1.12 s^{-1}, which was over 3.6 and 120 times higher than those of the 7.0 nm and 230 nm $Ni(OH)_2$ layers, respectively. Due to the uniform thickness across the entire wafer area, the $Ni(OH)_2$ nanosheet also exhibited excellent operational stability. This is the first report of wafer-scale ultrathin $Ni(OH)_2$ nanosheet, which exhibited drastically enhanced electrochemical catalytic activity. This work offers a promising new catalyst solution for water splitting. The ILE technology for synthesizing wafer-scale oxide 2D nanomaterials is exceptionally valuable for developing catalysts with unprecedented mass activity from rare and precious catalyst materials.

4. Ionic Layer Epitaxy of Nanometer-Thick Palladium Nanosheets with Enhanced Electrocatalytic Properties

The quasi-2D morphology of Pd was demonstrated as an efficient catalyst owing to the high surface area/volume ratio with a myriad of active sites exposed and rapid charge transport across the ultrasmall thickness. Due to the nonlayered face-centered cubic (fcc) crystal structure of Pd, it is still fairly challenging to synthesize Pd nanosheets with well controlled size, thickness, and crystal facets, which are critical to rational design of catalytic activities. Prevailing method of synthesizing Pd nanosheets was relying on selective absorption of surfactants to restrict the out-of plane growth. However, due to the limited sizes of surfactant micelles assembled in bulk solution, these strategies often yielded very small particle sizes.

In ILE, a self-assembled amphiphilic monolayer at the water−air interface was used as a soft template to guide the nucleation and growth of 2D nanosheets underneath. The packing density of amphiphilic molecules in the monolayer controls the thickness of the nanosheet with a resolution down to one unit cell. It is hypothesized that if an appropriate pair of amphiphilic molecule and aqueous synthesis protocol is identified, it will be possible to grow 2D metal nanosheets by ILE with control thickness and large sizes. In this work, we demonstrated a successful ILE growth of ultrathin Pd nanosheets using an oleylamine monolayer at the water−air interface. The Pd nanosheets exhibited a quasi-square shape and a tunable thickness from 2.0 to 3.2 nm. Owing to the ultrasmall thickness, high crystallinity, and exposure of active crystal facets, the Pd nanosheets demonstrated a more than 30 times higher catalytic activity compared to the commercial Pd black. This work offered a promising approach toward rational design and synthesis of ultrathin metallic 2D nanosheets with enhanced functionality.

In the growth process, the ionized oleylamine molecules self-assembled into a positively charged monolayer at the water−air interface. Negatively charged anionic groups (e.g., $PdCl_4^{2-}$) were attracted to the interface, forming an ultrathin precursor-concentrated region beneath the monolayer. At an elevated temperature of 60 ℃ and in the presence of a reducing agent (HCHO), Pd crystals were nucleated and grown within the confined region forming 2D nanosheets. The crystal structure of Pd nanosheets was characterized by transmission electron microscopy

(TEM). The ultrathin nanosheets remained its original shape after being transferred to the holey carbon TEM grid. Selective area electron diffraction (SAED) pattern collected from the nanosheet region showed a clear polycrystalline feature (Figure 7). The concentric diffraction rings could be indexed to {200}, {311}, and {222}, matching well to the JCPDS card (No. 46-1043), further confirming the metallic fcc Pd structure. High-resolution TEM (HRTEM) image revealed the nanosheet was composed of crystalline domains with a size of 10−15 nm. These domains exhibited different orientation but all had the same thickness. This growth phenomenon further confirmed the ILE mechanism that nanosheet nucleation and growth is confined within the nanometer thick precursor-concentrated region underneath the amphiphilic monolayer, regardless of the crystal orientation. Based on the oriented attachment principle, the polycrystalline feature was likely because the bonding force between Pd atoms was not high enough to overcome the environmental resistance for domain rotation, particularly the strong steric hindrance from the carbon tails of oleylamine in the monolayer. HRTEM of a single domain revealed a clear and sharp lattice of the Pd crystal, and no indication of amorphous or disordered region could be observed. The corresponding fast Fourier transform (FFT) pattern confirmed the crystalline domain had an exposed (101) surface plane. The lattice spacing of the (020) and (111) planes were measured to be 0.19 and 0.22 nm, respectively. The high-energy (100) facet was also observed coexisting with the (101) facet (Figure 7C). The orientation was confirmed by FFT (inset of Figure 7C). Exposure of the highly active (001) facets was favorable for the Pd nanosheets to show enhanced catalytic performance. The energy-dispersive X-ray spectrum (EDX) taken from the nanosheet showed a strong Pd signal (Figure 7D), while only negligible O signal was detected. EDX elemental mapping showed that the Pd signal clearly outlined the shape of nanosheet (Figure 7F), whereas the O signal was uniformly distributed over the entire carbon supported area (Figure 7G). The structural and elemental characterizations confirmed that the nanosheets were pure metallic Pd phase with no oxidation features involved.

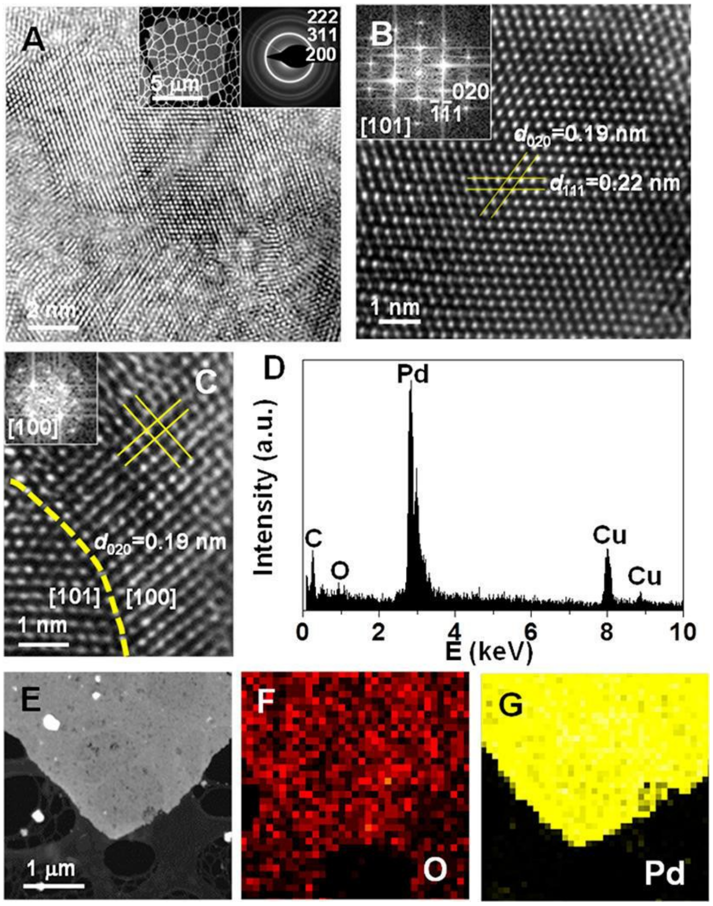

Figure 7. Crystal structure and composition characterization of the nanosheets. (A) HRTEM image showing the crystalline domains with different crystallographic orientation. Inset is the corresponding selective area electron diffraction pattern. (B) HRTEM image on one crystalline domain showing a perfect (101) crystal facet without any observable defects. Inset is fast Fourier transform pattern (FFT). (C) HRTEM image showing two crystalline domains with the exposed (101) and (100) facets. A grain boundary is indicated by a yellow dashed line. Inset is FFT of the (100) facet. (D) EDX spectrum. (E) Low-magnification TEM image and corresponding EDX elemental mapping of (F) O and (G) Pd.

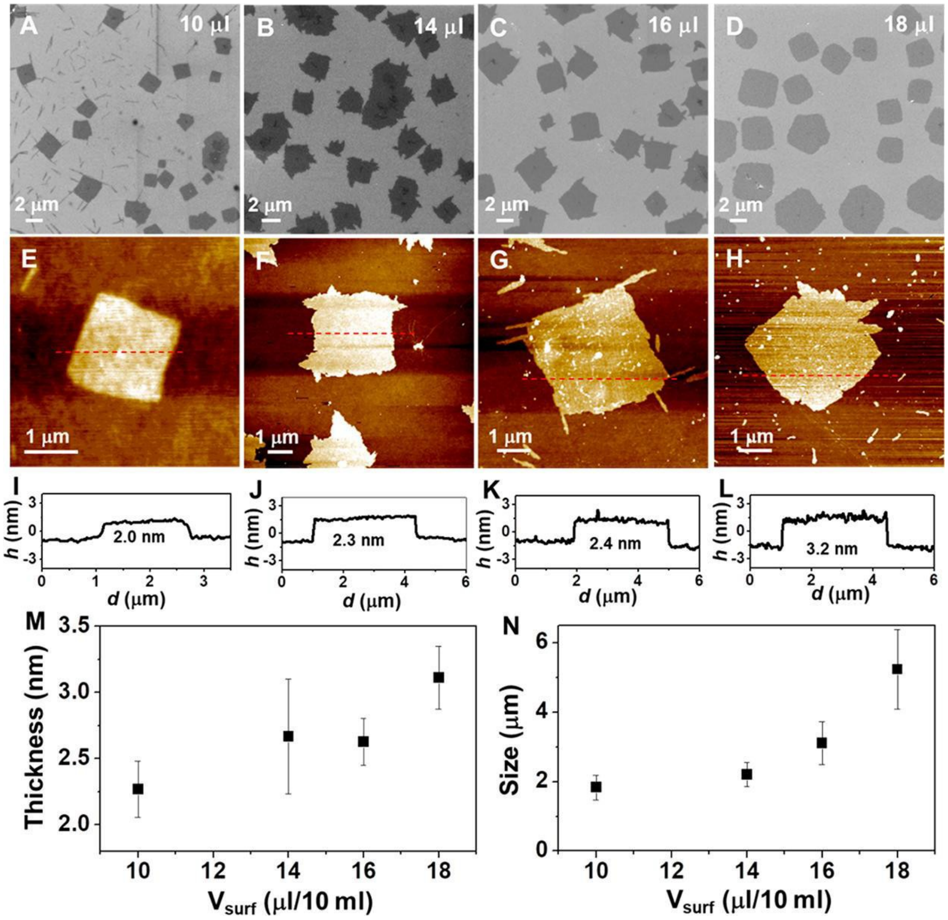

Figure 8. Influence of the oleylmaine monolayer packing density on the size and thickness of Pd nanosheets. (A−D) SEM images, (E−H) AFM topography images, and (I−L) height profiles along the red dashed lines in corresponding AFM topography images of Pd nanosheets grown with (A, E, I) 10 µL, (B, F, J) 14 µL, (C, G, K) 16 µL, and (D, H, L) 18 µL chloroform solution of oleylamine. (M, N) Plots of (M) the thickness and (N) the size as functions of volume of chloroform solutiom of oleylamine. Each dot is the average value of 20 sets of experimental data, and error bars show standard error.

The packing density of ionized amphiphilic monolayer had strong influences on the width of precursor-concentrated region and thus could finetune the nanosheet thickness. To test this principle in the Pd nanosheet growth system, four packing densities were used, which are 3.61 × 10^{-5}, 5.04 × 10^{-5}, 5.77 × 10^{-5}, and 6.49 × 10^{-5} mol/m^2, respectively. All of packing densities yielded Pd nanosheets with similar quasi-square geometry Figures (8A−D). The nanosheet densities were nearly unchanged, but the size of nanosheets obviously increased as the packing density increased. The AFM topography images (Figures 8E−H) and corresponding height profiles (Figures 8I−L) further revealed the morphology change as a function of the surfactant packing density. All the nanosheets exhibited an equivalently good surface flatness (Ra = 0.20

nm) and uniform thickness, evidencing the high reproducibility of ILE in 2 nanosheet. As the packing density increased, the nanosheet thickness raised monotonically from 2.0 nm to 2.3, 2.4, and 3.2 nm. Further statistical analysis of over 20 nanosheet samples revealed a correlation between the nanosheets' thickness and size and the surfactant packing density, consistent with those observed from the growth results of ZnO nanosheets (Figures 8M and 8N). The thickness of Pd nanosheets increased from 2.3 ± 0.2 to 3.1 ± 0.2 nm as a functional of the packing density. Meanwhile, the side length increased accordingly from 1.83 ± 0.36 μm to 2.20 ± 0.35, 3.11 ± 0.62, and 5.24 ± 1.14 μm. This size and thickness increase following the packing density of surfactant monolayer was an immediate result of the enriched precursor ion concentration in the nanosheet nucleation region, which is a primary ILE growth kinetics.

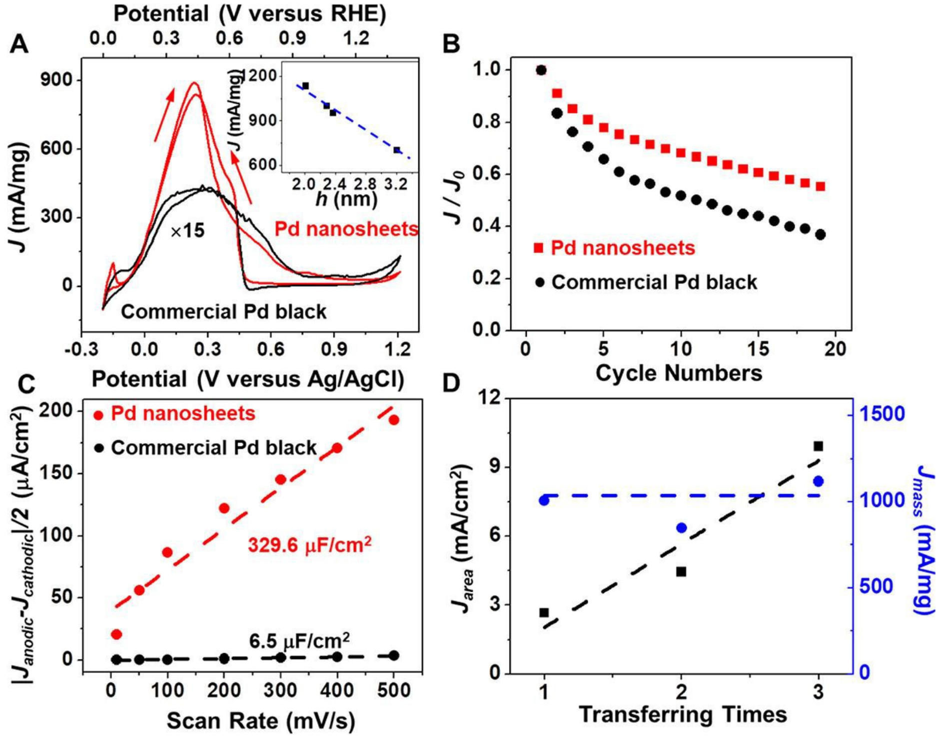

Figure 9. Electrocatalytic activities of palladium nanosheets for the oxidation of formic acid. (A) Current density (mass)−potential curves and (B) stabilities of palladium nanosheets and commercial palladium black as a comparison recorded in an aqueous solution containing 0.5 M H_2SO_4 and 0.25 M HCOOH at a scan rate of 50 mV s^{-1} . Inset shows the dependence of current density on the thickness of nanosheets. Straight blue dashed line serves as a guide to the eye. (C) Plot showing the extraction of the double-layer capacitance (Cdl) for palladium nanosheets and commercial palladium black. The dashed lines are linear fitting curves, with the slopes revealing Cdl. (D) Dependence of area current density (I_{area}) and mass current density (I_{mass}) on transferring times of palladium nanosheets from water−air interface to the substrates by scooping. Straight blue and black dashed lines serve as guides to the eye.

Pd has been considered as an efficient anodic, monometallic electrocatalyst for formic acid oxidation (FAO) in a direct formic acid fuel cell. Figure 9A shows the mass current density−potential curves measured in an aqueous solution consisting of 0.5 M H2SO4 and 0.25 M HCOOH at a scan rate of 50 mV s−1. The broad peaks at 0.23 V (versus Ag/ AgCl) that appeared in both forward and reverse scan represented the direct oxidation of formic acid to CO_2. According to the Nernst equation, the thermodynamic potential at this FA concentration was estimated to be −0.181 V (versus RHE). Thus, the overpotential for Pd nanosheets was calculated to be 0.288 V (versus RHE). The corresponding potentials versus RHE were shown by using top x-axis in Figure 9A. As compared, the curve of the commercial Pd black shared the similar shape in both forward and reverse scan, with a slightly higher overpotential 0.308 V (versus RHE). However, the maximum mass current density of Pd nanosheets reached as high as 895.5 mA/mg at 0.23 V (versus Ag/AgCl), roughly 31 times larger than the commercial Pd black (~28.8 mA/mg at 0.23 V versus Ag/AgCl). This value is also much higher than many Pd nanostructures reported in the literature, such as Pd nanoparticles (190 mA/mg), 3D Pd nanoflowers (211.3 mA/mg), Pd tetrahedra (450 mA/mg), and Pd-based alloys (510 mA/mg) and at the same level of other Pd nanoplates with a similar thickness but much smaller sizes. Despite the ultrasmall thickness, the Pd nanosheets exhibited a superior stability compared to commercial Pd black. As shown in Figure 9B, after catalyzing FAO in the acid solution for 20 cycles, the maximum oxidation current of the Pd nanosheets decreased to 56% of the initial value, whereas the commercial Pd black only maintained 37% of the initial value. The higher stability of Pd nanosheets could be potentially attributed to the stronger adhesion to the substrates due to the large and ultraflat contact area as compared to Pd black particles, which prohibited Pd nanosheets from dissolution or aggregation during the catalytic reactions. The outstanding catalytic performance was attributed to the ultrahigh ratio of surface active sites to bulk volume arisen from the ultrathin feature. This merit was verified by measuring the double-layer capacitance (Cdl), which serves as an estimation of electrochemically active surface area. As shown in Figure 9C, Pd nanosheets showed a Cdl of 329.6 $\mu F/cm^2$, 50.7 times higher than the commercial Pd black (Cdl = 6.5 $\mu F/cm^2$). This comparison confirmed that Pd nanosheets had a much higher specific electrochemically active surface area. In addition, given the monometallic and polycrystalline nature of the Pd nanosheets, the catalytic activity could be primarily attributed to the total exposed surface area rather than other geometric factors such as edges or side facets. Considering the surface coverage of Pd nanosheets was much lower than 100%, the surface catalytic performance can be further improved by multiple-time transfer. Accordingly, the area current density increased linearly by 3.65 mA cm^{-1} per transfer (Figure 9D, black curve). This incremental amount was nearly the same as the initial value, suggesting each transfer could introduce the same amount of catalytic active sites. Normalized by the mass of the nanosheets, the current density remained at the same value of 1005.4 mA/mg (Figure 9D, blue curve). The constant mass current density suggested that all the nanosheets contributed the same to the catalytic reaction regardless of their sequence and location of being transferred.

5. Ion layer epitaxy (ILE) ZnO nanosheets at the water-oil interface with highly-concentrated Zn vacancies

Ferromagnetism is an important material's property that could enable a broad range of applications, including spin transistors, spin light-emitting diodes, non-volatile memory, and logic devices. The ferromagnetism observed in doped/undoped ZnO was generally very weak due to the limited concentration of defects in the lattices. Bringing the crystal down to a 2D geometry may dramatically change the defect configuration and significantly enlarge the ferromagnetism. While ZnO is not a typical 2D crystal, which generally form in compounds with weak van der Waals bonding between layers, recent development of ionic layer epitaxy (ILE) successfully created single crystalline ZnO nanosheets with a nanometer-scale thickness, enabling ferromagnetism study in this new material system. Here, a monolayer of ZnO nanosheets with an average thickness of ~1.8 nm was synthesized at the water-oil (toluene oil phase) interfaces via ILE. These nanosheets were polycrystalline with domain sizes of ~10 nm.

After annealing in Ar, these nanosheets exhibited unprecedentedly strong Ms (57.2 emu/g) at both low temperature (4 K) and room temperature. Furthermore, single-crystalline ZnO nanosheets, grown by ILE at the water-air interface, exhibited a smaller but still unprecedented Ms of 37.2 emu/g. This strong ferromagnetism is attributed to the existence of a very high concentration of zinc vacancies. Density Functional Theory (DFT) study further demonstrated the extremely thin feature and the grain boundaries are favorable for the formation of VZn. These ZnO nanosheets with strong room-temperature ferromagnetism provide a promising new 2D material candidate for spintronic devices.

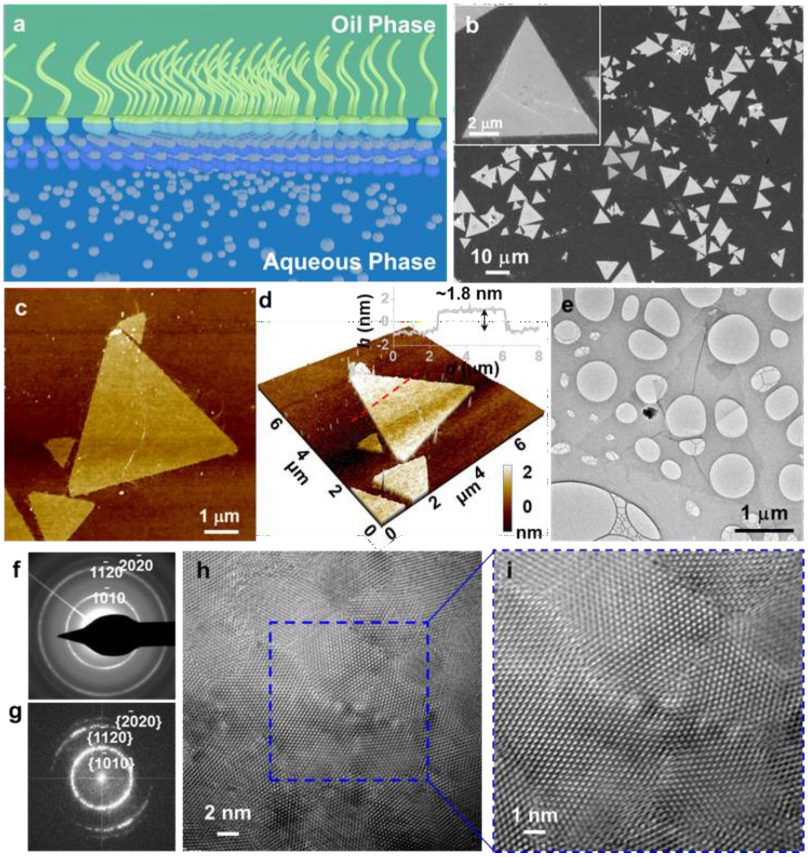

Figure 10. Morphology and crystal structure characterization of ZnO nanosheets grown at a water-oil interface. (a) Schematic of the water-oil interface. Yellow balls with a tail represent the surfactant monolayer. White balls are Zn^{2+} ions and blue balls are O^{2-} ions. (b) A large-scale SEM image showing the ZnO nanosheets on a Si substrate. Inset shows one triangular individual nanosheet. (c) AFM topography image showing the flat surface. (d) The corresponding 3D AFM image of the same nanosheet in (c). Inset is the height profile along the red dashed line revealing the thickness to be 1.8 nm. (e) Low magnification TEM image showing one nanosheet rested on a holey carbon TEM grid. (f) SAED pattern of the nanosheet. The concentric diffraction rings indicate the nanosheet is polycrystalline. (g) Corresponding fast Fourier transform pattern of the nanosheet. (h) High resolution TEM image showing the crystal lattice of wurtzite ZnO with grain boundaries. (i) Enlarged TEM image of (h) showing the grains separated by the grain boundaries.

The ZnO nanosheets were synthesized by ILE using a new water-oil interface instead of the conventionally used water-air interface. As schematically shown in Figure 10a, the water-oil interface was formed by using an aqueous ZnO nutrient solution as the water phase and toluene as the oil phase. The surfactant monolayer of sodium oleylsulfate (NaO4SC18H35) stabilized itself at the water-oil interface by keeping the hydrophilic head groups in the water phase and the hydrophobic tails in the oil phase. The ionized surfactants were negatively charged and attracted the positively charged Zn^{2+} cations to form a concentrated ionic layer underneath the headgroups. The monolayer then served as a template to direct the nucleation and growth of the nanosheets within the concentrated Zn^{2+} layer. Similar to the growth results from typical water-air ILE, the as-prepared ZnO nanosheets all had a triangular shape (Figure 10b). Most nanosheets exhibited a side length of ~10 μm, while smaller nanosheets with sizes of 2-3 μm were also observed. As shown by a typical example in the inset of Figure 10b, the nanosheets had sharp and equal-length edges, and clean surfaces. Atomic force microscopy (AFM) topography image in Figure 10c demonstrates the uniform thickness across the entire nanosheet, which was measured to be ~1.8 nm. One significant outcome from the water-oil interface ILE is the very clean surfaces with fewer particles and surface additives as compared to the water-air interface growth. This feature can be clearly observed from the 3D topography shown in Figure 10d. The improved growth cleanness can be attributed to the less dynamic water-oil interface at the growth temperature (60 ℃) compared to the water -air interface.

The crystal structure of the nanosheets grown at the water-oil interface was analyzed by electron microscopy. Figure 10e shows a low magnification transmission electron microscopy (TEM) image of an individual nanosheet resting on a holey carbon TEM grid. A striking feature from these nanosheets was their polycrystalline structure, as revealed by the concentric diffraction rings from the selected area electron diffraction (SAED) (Figure 10f), which was completely different from the single-crystalline structure of the nanosheets obtained at water-air interface. The concentric diffraction rings were indexed to {10 0}, {11 0}, and {20 0}, matching well to the JCPDS card (No. 36-1451), confirming the hexagonal wurtzite structure. The fast Fourier transfer (FFT) pattern in Figure 10g showed the same diffraction rings as that in Figure 10g. The composition of the nanosheet was confirmed by X-ray photoelectron spectroscopy (XPS), where Zn 2p peaks emerged at 1024 eV and 1048 eV, O 1s peak at 534 eV, consistent with those in wurtzite ZnO. The high resolution TEM (HRTEM) image in Figure 10h clearly shows the polycrystalline lattice, where the irregular crystalline domains had sizes of ~10 nm in average. A closer observation in Figure 10i revealed the clean wurtzite lattices of all the domains with exposed (0001) surface. The domain boundaries were sharp and no amorphous phase could be found in between. Formation of the polycrystalline structure could be attributed to the higher steric hindrance provided by the oil phase. This is because the formation of single-crystalline nanosheets is a result of free rotation of crystallites as they merge via the oriented attachment mechanism, where the surfactant tails in air had a much lower energy barrier for lateral movement. Molecular dynamics (MD) simulation was used to further understand how the surfactant-oil phase interaction influences the nanosheet growth. With the same surfactant density and Zn^{2+} ion concentration, the surfactant monolayer at water-oil interface exhibits a relatively higher roughness compared to the water-air interface, as surfactants are pulled more toward the oil phase. This might be the reason that the water-oil interfaces yielded smaller nanosheets. Based on the MD results, the charge density induced by the ionized surfactant at the interface is plotted and compared. Ionized surfactants at water-oil interface yielded ~28% lower charge density compared to that at the water-air interface. As a result, the width of the Stern layer (Zn^{2+}-concentrated zone) at the water-oil interface was ~45% narrower than that at the water-air interface. Therefore, thinner nanosheets with a narrower thickness distribution were obtained from the water-oil interface.

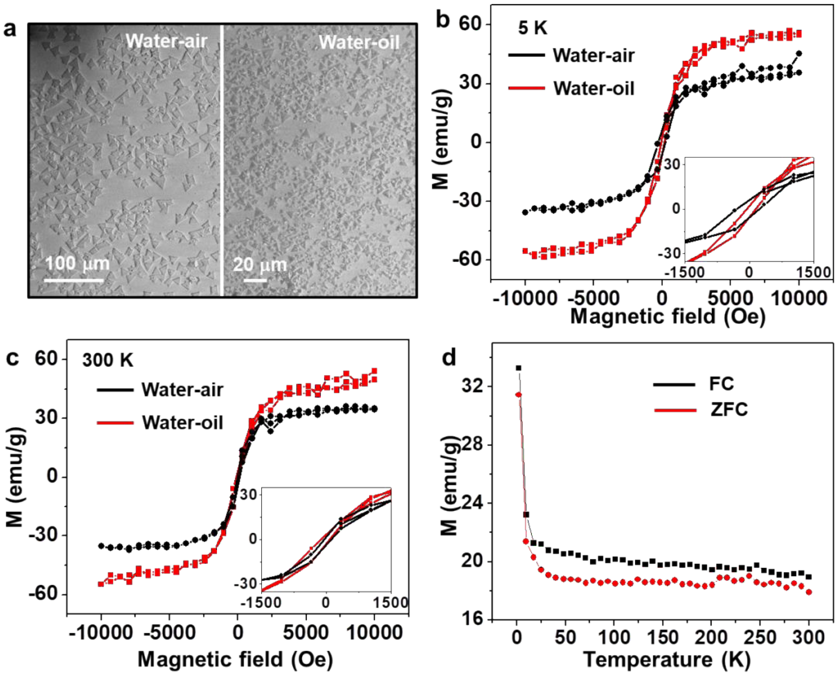

Figure. 11 Magnetic properties characterization of ZnO nanosheets. (a) Large-scale SEM images of ZnO nanosheets grown at the water-air interface (Left) and water-oil interface (Right) on sapphire substrates. Magnetization curves of the nanosheets at the water-air and water-oil interface at (b) 5K and (c) 300 K. The insets show the hysteresis loops at (b) 5K and (c) 300K. (d) Magnetization of the nanosheets at water-oil interface as a function of temperature from 5 K to 300 K. The applied magnetic field was 500 Oe.

The magnetic property of ZnO nanosheets was measured from a monolayer of densely distributed nanosheets supported on single-crystalline Al_2O_3 substrates. The large-area SEM images in Figure 11a show the coverage and distributio of ZnO nanosheets obtained from water-air and water-oil interfaces. Statistic measurements from five randomly selected areas of 150 x 250 μm^2 gave the surface coverages of 60.1±2.6% and 62.7±3.1% (errors are standard deviation between the measurements) for the water-air and water-oil nanosheets, respectively, which correspond to 9.9×10^{-7} and 6.5×10^{-7} g/cm^2. The magnetic response was measured as a function of magnetic field strength at both 5 K and room temperature using superconducting quantum interference device (SQUID), where the magnetic field was applied parallel to the nanosheets. After being annealed in Ar at 400 °C for 1 hour, strong ferromagnetism was discovered from both samples at 5 K and 300 K, as shown in Figure 11b and Figure 11c. The polycrystalline ZnO nanosheets grown at the water-oil interface showed a Ms of 57.2 emu/g at 5 K and 50.9 emu/g at 300 K. As a comparison, the single-crystalline ZnO nanosheets grown at the water-air interface showed smaller Ms of 37.2 emu/g at 5 K and 35.0 emu/g at 300 K. The small difference of Ms at 5 K and 300 K suggests the ferromagnetism is robust against thermal fluctuations in the range of 5 ~ 300 K. The temperature-dependent magnetization is further probed by the zero field cooled (ZFC) and field cooled (FC) measurements. As shown in Figure 11d, the nonzero difference between ZFC and FC curves from 5 to 300 K further supports the existence of room-temperature ferromagnetism.

6. Bioinspired Synthesis of Quasi-Two-Dimensional Monocrystalline Oxides

Creating 2D nanomaterials from nonlayered functional materials such as oxides and nitrides still remains a grand challenge for material synthesis, which typically requires stabilization of crystal phases or structures far away from equilibrium. Ionic layer epitaxy (ILE) is a typical example that relies on the ionized head groups in an amphiphilic monolayer to establish an electrical double layer to self-confine the crystal growth within a 2D nanometer regime. Nevertheless, the self-assembled templates are always associated with irregular morphology and polycrystallinity. In nacre, layers of organic matrix assembled from chitin and proteins control formation of hexagonal aragonite platelets (Figure 12a). The natural presence of both negatively and positively charged amino acid residues (e.g., negative aspartate and glutamate, and positive lysine and arginine) in the protein assemblies play a key role in controlling the growth of aragonite. Inspired by the protein-based templates in biomineralization, in this work, we adopted mixed surfactants with positive and negative head groups to direct the ILE synthesis of 2D nanosheets.

In the growth process of CoO nanosheets, mixed anionic oleylsulfate (SOS) and oleylamine (OAM) surfactants self-assembled into a mixed monolayer with excess negative charges at the water−air interface. The ratio of the positive and negative surfactants has great effect on the morphology of the 2D nanosheets. When mono surfactant SOS was used, after 100 min of growth, a continuous polycrystal film was obtained at the water-air interface (Figure 12c), as in most previous ILE studies of oxides. When mixed surfactants with mole ratio of SOS/OAM = 9:1 was used, there appeared a single layer of triangular nanosheet array that covered the entire water-air interface. The as-prepared ultrathin nanosheets retained their original shape after being transferred to the holey carbon TEM grid (Figure 12e). Selected area electron diffraction (SAED) pattern collected from the nanosheets showed a clear monocrystalline feature with a perfect hexagonally arranged diffraction spots (inset of Figure 12e), which could be indexed to the (110) and (100) facets of β-$Co(OH)_2$. The single crystal $Co(OH)_2$ nanosheets could be directly transformed to CoO by O_2 plasma treatment without changing the triangle morphology (Figure 12f). High resolution TEM (HRTEM) image showed the (200) d-spacing measured to be 0.21 nm (Figure 12g). Energy-dispersive X-ray spectroscopy (EDS) mapping in the corner area marked by the orange box in Figure 12e showed a uniform distribution of oxygen and cobalt elements in the nanosheet (Figure 12h, i). All the nanosheets exhibited a uniform thickness of 2.1 nm (inset of Figure 12j).

Statistical analyses of the nanosheet size distribution revealed a linear relationship between the side length and the reaction time, which increased from 1.0±0.7 μm at 25 min to 12.5±2.0 μm at 60 min (Figure 13a). In contrast, there was an initial sharp jump in the number of the nanosheets, followed by a slow rise during the remaining growth time (Figure 13b). A small increase of the nanosheet thickness (from 1.3 nm at 30 min to 2.7 nm at 300 min) was also observed from the topography AFM measurements (Figure 13c). The time-dependent morphological analyses suggested that the nanosheet nucleation and growth under mix-charges surfactant was similar to the classic LaMer model, where the nucleation of nanosheets was driven by the supersaturation of precursor within the 2D confined ionic layer, followed by the primary lateral growth of individual nuclei. This mechanism is strikingly different from that occurring in the single surfactant system. When only SOS surfactants were used, irregular nuclei nanostructures were formed after a relatively shorter incubation period. These initial nuclei connected to each other forming a network, which further grew into a continuous film.

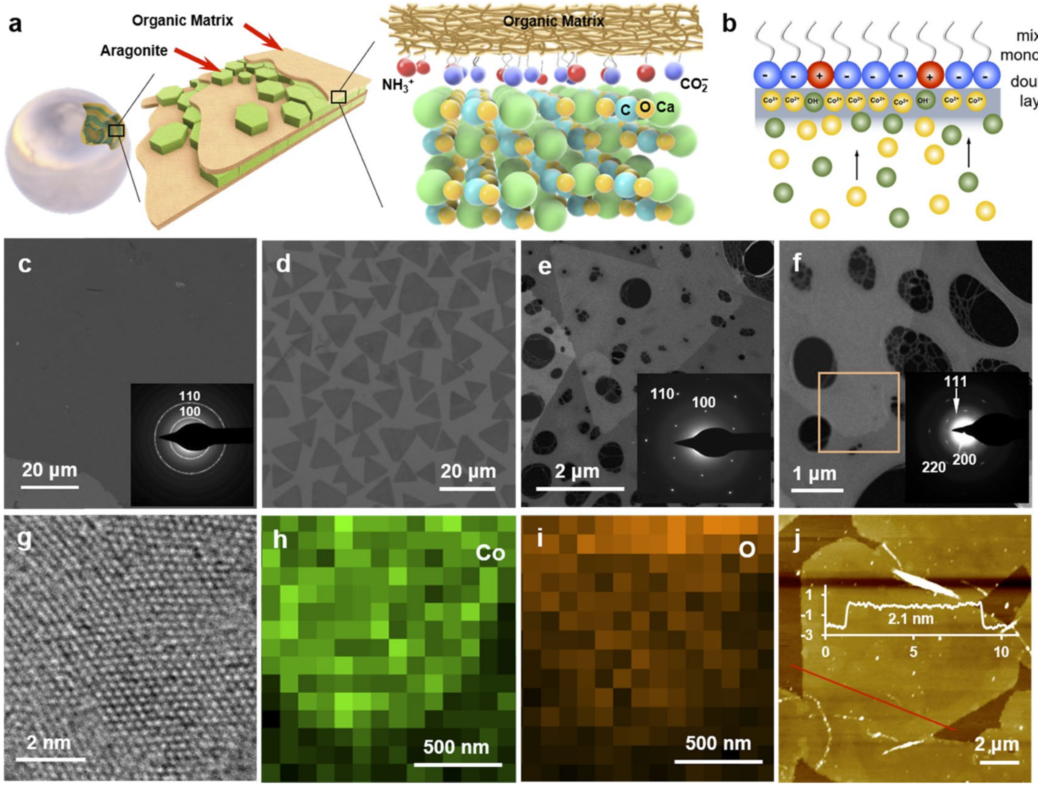

Figure 12. Nanosheet synthesis under mixed surfactants with opposite charges. (a) Layered structure of hexagonal aragonite platelets alternating with the organic matrix in the nacreous layer of pearl and the schematic representation of the protein surface structure with well-mixed positively (red) and negatively (blue) charged amino acid residues directing the biomineralization of aragonite. (b) Schematic illustration of the formation of monocrystalline nanosheets with the mixed monolayer bared positive (red) and negative (blue) charges on the interface of the precursor solution and air. (c) SEM image of the continuous film of Co(OH)2 synthesized with mono SOS as transferred to a SiO2/Si substrate surface. The inset is the selected area electron diffraction (SAED) pattern of the synthesized film, which indicated the polycrystallinity of the film. (d) SEM image of a triangular Co(OH)2 nanosheet synthesized with a mixed monolayer (SOS/OAM = 9:1) as transferred to a SiO2/Si substrate surface. (e) Low magnification TEM image and the selected area electron diffraction (SAED) pattern (inset) of the triangular nanosheet rest on a holy carbon TEM grid. (f) Triangular nanosheets after 10 min of O2 plasma treatment. The inset is the SAED pattern, which matches well with the CoO structure. (g) High-resolution TEM image showing the crystal lattice of CoO after plasma treatment of the triangular nanosheets. Elemental mapping of (h) cobalt and (i) oxygen in the area of triangular nanosheets marked by the orange box in (f). (j) Topography atomic force microscopy (AFM) image showing the nanometer thickness and good surface flatness of the nanosheets. The inset is the height profile along the red line revealing that the thickness is 2.1 nm.

The evolution of 2D crystals under different surfactant monolayers was further analyzed in-situ using grazing incidence X-ray diffraction (GID) (Figure 13d-13g). For mixed SOS/OAM monolayer (SOS/OAM = 9:1), short diffraction rod at $Q_{xy} = 2.285$ Å^{-1} (d = 2.75 Å) with the same d-spacing as (100) plane of β-$Co(OH)_2$ was observed. The presence of straight and sharp diffraction rods confirmed that all nanosheets were 2D monocrystals with their (001) planes oriented parallel to the water surface. Under mono SOS monolayer, a diffraction ring at $Q_{xy} = 2.285$ Å^{-1} (Q_z=0) appeared instead of the short straight rod. It was a clear signature that the system became polycrystalline and that the crystallite (001) planes were oriented randomly with respect to the water surface.

Molecular dynamics (MD) simulations were performed to model the mixed monolayer at the water/vacuum interface and its interaction with Co^{2+} in water. In an equilibrated monolayer, the positively charged OAM was agglomerated into small regions within the negatively charged SOS matrix, forming OAM rich and OAM poor regions. At the OAM rich regions, the Co^{2+} concentration underneath was significantly lower compared to the OAM poor regions. The regions low in Co^{2+} concentration could form boundaries that confine and isolate nucleation of nanosheets into small zones and thus prevent agglomeration at the nucleation stage. MD simulations have also shown that mixed surfactants are able to form a flatter monolayer at the water-vacuum interface than mono SOS surfactants. The roughness of mix-charges monolayer is nearly constant as a function of Co^{2+} concentration, whereas roughness of the mono-surfactant increases with decreasing Co^{2+} concentration (blue curve in Figure 13j). That means that as the nanosheets nucleate and Co^{2+} concentration decreases, the SOS monolayer may become gradually distorted, introducing defects into the nanosheets. Experimentally, the mix-charges surfactant monolayer showed better ordering, as indicated by FTIR spectra obtained from mixed monolayer in the presence of Co^{2+} ions after transferring onto Al_2O_3 substrates. The symmetric and antisymmetric stretching vibrations of the methylene groups was observed from mono SOS surfactant at 2854 and 2927 cm^{-1}, respectively (Figure 13k). However, these two peeks peaks shifted to 2850 and 2918 cm^{-1}, respectively, when SOS was mixed with OAM at 9:1 ratio. This shift to lower wavenumber indicated a more ordered structure of the alkyl tails in the surfactant monolayer.

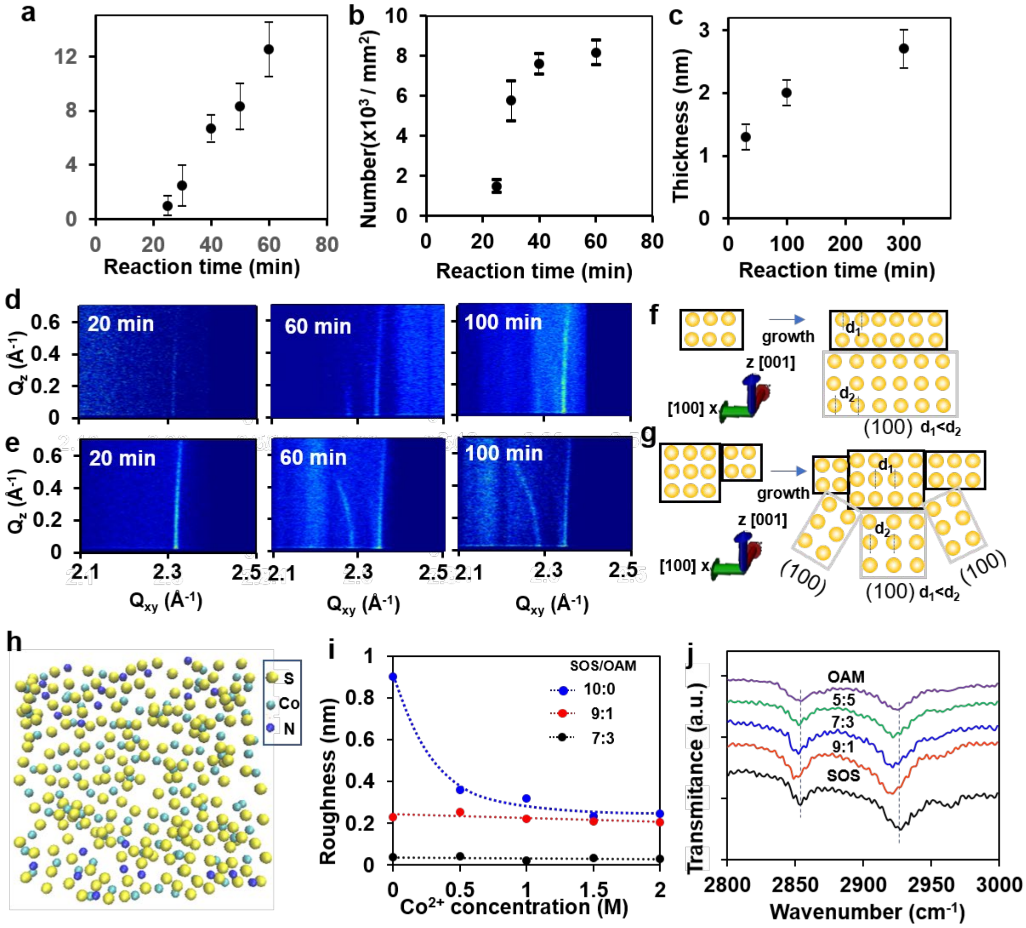

Figure 13. Growth process of a single-crystal triangular nanosheet of $Co(OH)_2$ under mixed monolayers. (a) The average edge length of triangular nanosheets at different reaction time. (b)

The average number of triangular nanosheets per millimeter square at different reaction time. (c) The thickness of the triangular nanosheets at different reaction time. (d) Grazing incidence X-ray diffraction (GID) data collected for in situ single-crystal triangular nanosheet growth under the mixed monolayer (SOS/OAM = 9:1) at the different reaction time of 20, 60, and 100 min. (e) GID data collected for in situ polycrystalline film growth under the monolayer of mono SOS at the different reaction time of 20, 60, and 100 min. (f) Schematic illustration of the nanosheet crystal evolution under the guide of mixed surfactant. (g) Schematic illustration of the nanosheet crystal evolution under the guide of mono SOS. (h) MD simulation-generated surfactant distribution of the mixed monolayer of SOS (S) and OAM (N) (SOS/OAM = 9:1) at the water/vacuum interface with 5 mM Co^{2+} in water. (i) Roughness of monolayers as a function of Co^{2+} concentration in the adjacent solution for SOS (blue), SOS/OAM = 9:1 (red), and SOS/OAM = 7:3 (black). (j) IR spectra of the mixed monolayer with Co^{2+}.

The synthetic strategy of adapting mix-charges surfactants to template crystal growth is generic and can be applied to synthesizing ultrathin 2D nanosheets from a myriad of multi valance metal oxides. As shown in Figure 14a, by using the same SOS/OAM mixture (9:1) at the water/air interface, it was possible to synthesize square shaped Bi_2O_3 nanosheets. They exhibited edge lengths of 1-2 μm and thickness of 4.5 nm (Figure 14b). HRTEM and corresponding SAED pattern confirmed the monocrystallinity of the cubic Bi_2O_3 nanosheets. Mixing OA and OAM at a ratio of 9:1 was used to form 2D hexagonal MnO_2 nanosheets (Figure 14d) in acidic condition. The MnO_2 nanosheets exhibited a uniform hexagonal shape with sizes in the range of 1-2 μm and thicknesses of ~ 2 nm (Figure 14e). They were monocrystalline and the lattice was identified as the hexagonal birnessite (Figure 14f), well represented by the shape of the nanosheets. In addition to pure-phased oxides, the mix-charges monolayer could also be used to introduce dopants to oxide nanosheets. Using mixed nickel and zinc ions solution as precursor under the SOS/OAM monolayer at a ratio of 7:3, monocrystalline Ni-doped ZnO nanosheets were successfully synthesized (Figure 14g). All the nanosheets exhibited a uniform thickness of 2 nm (Figure 14h). EDS elements mapping con-firmed the uniform distribution of Ni atoms within the triangular nanosheet. HRTEM and corresponding SAED pattern confirmed the monocrystalline structure of wurtzite ZnO (Figure 14i). While it is extremely challenging to uniformly dope nanosheets at the nanometer scale, the mix-charges surfactant opened a unique route toward doping 2D nanomaterials with-out influencing its morphology and monocrystallinity. Beyond the all-solution-based synthesis conditions, the mix-charges surfactant ILE could be extended to a gas-liquid reaction system, with which thin films of crystalline Fe_3O_4 was synthesized. The mixed monolayer of 1-octadecanol and OAM (1-octadecanol/OAM = 19:1) directed the growth of iron oxides films by reacting Fe^{2+} with NH_3 gas at the interface under room temperature. Due to the weak anionic properties of the 1-octadecanol, the mixed templates showed less stability than ionic mixtures of SOS and OAM, thus leading to irregular film formation (Figure 14j). Nevertheless, the thickness of the film was maintained around 2.5 nm (Figure 14k). HRTEM revealed formation of monocrystalline domains of the Fe_3O_4 (Figure 14l).

By learning from biomineralization, we introduced mix-charges surfactant template with positive and negative head groups to direct the ILE synthesis of large-area, single-crystalline nanosheets. This unique free-standing template enabled the formation of monocrystals by inducing concentrated metal ion regions in the electric double layer and aligning the orientation of the facets. Mix-ing charges yielded a stable, flatter, and more ordered monolayer template with a non-uniform distribution of charges, which were able to tune the 2D crystal nucleation rate and promote the growth of monocrystalline domains. The mix-charges template showed great promises as a ver-satile synthesis paradigm for creating quasi-2D nano-materials from a wide range of oxides, beyond van der Waals solids. This new 2D nanomaterial system will lead to the emerging of new or enhanced physical properties such as ferromagnetism, superconductivity, and single photon emission

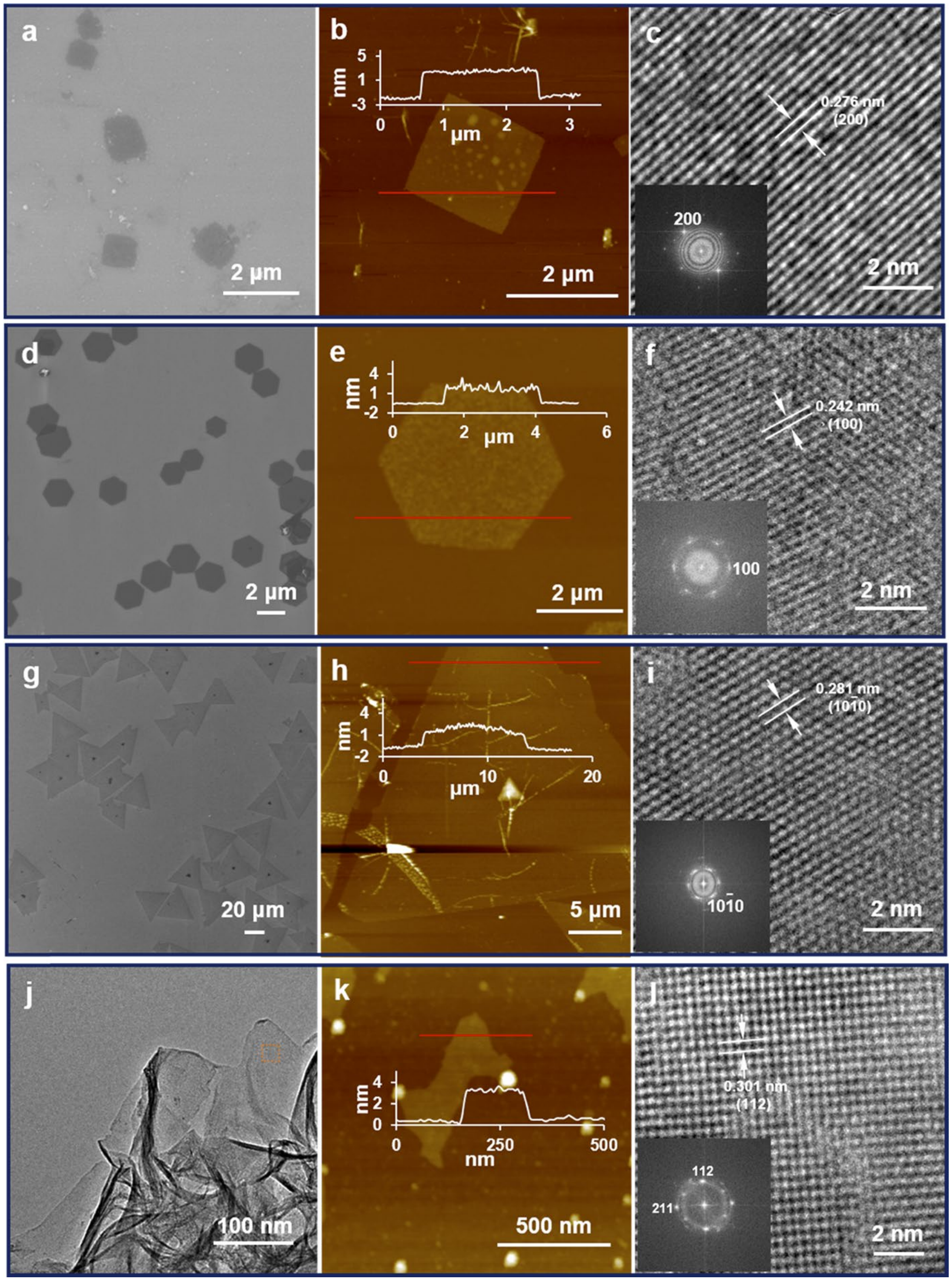

Figure 14. Morphology of single-crystal 2D nanosheets synthesized with mixed monolayers. SEM images (a, d, g), AFM topography images (b, e, h, k), TEM image (j), and high-resolution TEM images (c, f, i, l) of ultrathin 2D nanosheets for Bi_2O_3 (a−c), MnO_2 (d−f), Ni-doped ZnO (g−i), and Fe_3O_4 (j−l). The thickness profiles and SAED patterns of the four metal oxides are shown as the insets in (b, e, h, k, c, f, i, l).

7. Memristive Behavior Enabled by Amorphous-Crystalline Two Dimensional Oxide Heterostructure

The increasing demand of high density, non-volatile memory devices has been driving the development of nanoscale memory-bit cells. Metal oxides are the most intensively investigated for the memristive material due to their good chemical stability and broad selection of electrical properties. 2D nanomaterials offer a quantum-confined medium which can have exceptional transport properties and substantially improved memristive behavior compared to conventional bulk materials. Due to the unavailability of 2D oxides nanomaterials and the high entropy of introducing vacancies in 2D confined geometry, stable 2D oxide-based memristors have yet to be demonstrated.

Atomically thin single crystalline ZnO nanosheets were synthesized by ILE with sizes over ten microns, enabling the study of the memristor properties based on 2D metal oxides. ZnO nanosheets was transferred onto a Si wafer with 50 nm thermal oxide layer for device fabrication. Pre-patterned Ti/Au electrodes were deposited onto ZnO nanosheets by e-beam evaporation to form lateral Au-ZnO-Au (MIM) devices (Figure 15). The MIM structure had a wide space (~3 μm) between the two electrodes, where the thickness of the un-coated nanosheet channel was only ~0.75 nm as probed by an AFM scan. A 5-nm thin amorphous Al_2O_3 layer was then deposited on the surface of the entire ZnO nanosheet device by atomic layer deposition (ALD). The ALD-coated ZnO nanosheets exhibited a strong memristive behavior when the voltage was swept between ±10 V. Starting at 0 V, the device exhibited the high resistance state (HRS) with a very low current at the level of nA. As the voltage increased to ~8.75 V, the current abruptly jumped to above μA, switching to the low resistance state (LRS), *i.e.* the set process. By plotting $\ln J$ as a function of $V^{1/2}$, the transport characteristic within the HRS range fitted well to the Poole-Frenkel emission model within the voltage range between 0.5 to 2.5 $V^{1/2}$. The LRS I-V characteristic was fitted from 4 to 1 V^2 when the applied voltage was swept back to 0 V. The transport behavior fitted well with the Mott–Gurney law, indicating that the LRS was mainly controlled by space charge limited conduction (SCLC). According to the fitting curve, the carrier mobility was estimated to be ~2400 $cm^2V^{-1}s^{-1}$, by using $\varepsilon_r = 8.5$ and $d = 3$ μm. This value is the highest reported carrier mobility in semiconductor oxides.

Repeatability was studied through setting/resetting the device by pulse cycles for up to 10^6 times. The current at the LRS and HRS extracted from different pulse cycles showed good endurance, comparable to the typical endurance of commercial flash memories. The current was stable at 0.28 mA/mm at HRS and 5.42×10^{-5} mA/mm at LRS for 100 min without degradation. Compared to various memristive structures based on ZnO, our device showed an endurance among the highest values (10^6), while maintaining a large ON/OFF ratio and good retention performance. Most importantly, our device was able to reset at a low current (0.03 mA) and switch between HRS and LRS at low electric field ($2.9\text{x}10^6$ V/m), suggesting a good potential to achieve low power consumption. In contrast, most ZnO-based memristive devices exhibited high power consumption as a result of the high operation current (> mA).

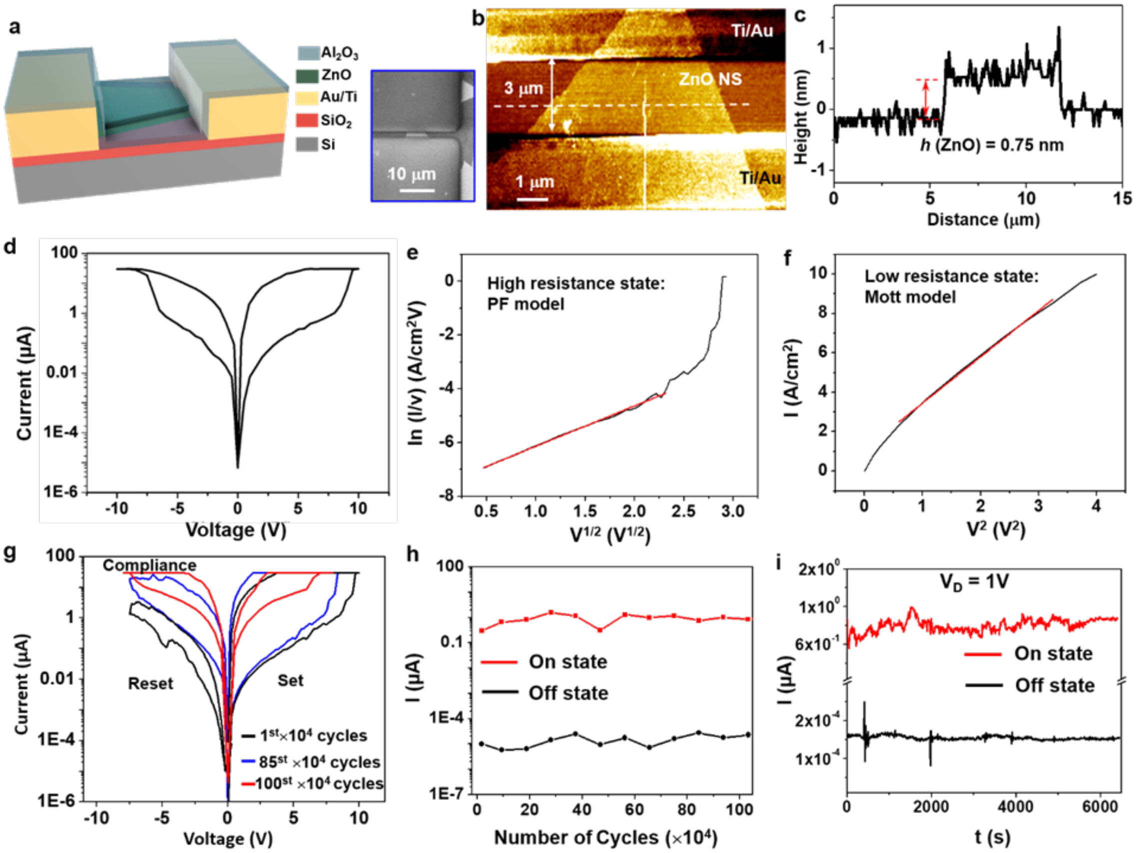

Figure 15. ZnO/Al_2O_3 Memristive Device Characterization. (a) Schematic of a ZnO/Al_2O_3 heterolayered nanosheet memristor. Inset: SEM image showing a conductor-oxide-conductor memristor consisting of two electrodes bridged by one nanosheet. (b) AFM topography image illustrating the channel width and length of one typical memristor. (c) Height profile showing the thickness of the nanosheet in (b) was 0.75 nm. (d) The logarithm scale of the I-V curve of ZnO/Al_2O_3 memristor. (e) Fitting curve at the HRS portion showing the Poole–Frenkel emission model as the conduction mechanism. (f) Fitting curve at the LRS portion showing Mott–Gurney behavior as the conduction mechanism. (g) Three I–V curves of the ZnO nanosheet memristor at 1×10^{4}th cycle, 85×10^{4}th cycle, and 100×10^{4}th cycle, showing the sustained memory behavior throughout a large number of cycles. (h) The endurance of one device over 10^6 cycles at “On” and “Off” states respectively. ~500 ns pulses were used for the device measurement. (i) The retention of the “On” and “Off” states over 100 min. A read voltage of 1 V was used for the measurement.

The low magnification STEM image in Figure 16a showed an as-synthesized triangular ZnO nanosheet (with brighter contrast) resting on a holey carbon TEM grid. The high resolution TEM (HRTEM) image in Figure 16b reveals the single-crystalline lattice with a typical hexagonal arrangement. Figure 16c shows that the morphology of the triangular nanosheet after Al_2O_3 coating was well maintained. The single-crystalline wurtzite crystal lattice was well preserved after the coating, and the sharp SAED pattern in the inset of Figure 16d further confirmed no other crystalline phase was introduced by ALD. The STEM image in Figure 16e is a cross-section through the heterojunction, showing three distinct layers of thick amorphous SiO_2, ~ 1 nm ZnO, and ~2 nm amorphous Al_2O_3. The corresponding element maps confirmed the well separated layers of Al (Figure 16f), Zn (Figure 16g), and Si in SiO_2 (Figure 16h). The result of depth profile from X-ray photoelectron spectroscopy matched well with layer configuration

($Al_2O_3/ZnO/SiO_2$).

Electron energy loss spectroscopy (EELS) results from cross section samples confirm that the Al_2O_3 coating induces O vacancies in the ZnO nanosheet. Figure 16j and 16k are the O and Zn edges, respectively, from an Al_2O_3-coated ZnO nanosheet. The Zn:O ratio is 1.37. The composition suggests a large concentration of O vacancies. The formation of the oxygen vacancies as a result of Al_2O_3 coating is proposed in Figure 16l. When the Al precursor (trimethylaluminum, TMA) is introduced to the ZnO nanosheets during ALD, it preferably bonds to the surface O ions, as the bonding energy of Al−O (511 kJ/mol) is significantly larger than that of Zn−O (159 kJ/mol). Due to the ultra-small thickness of our ZnO nanosheets, this surface effect would turn into a bulk property and fill the entire ZnO channel with concentrated O vacancies. Under an in-plane electric field, these O vacancies were able to diffuse and cluster together, forming continuous conductive filaments to carry a high electric current in between the two electrodes. The memristive behavior arises from high-speed drift of oxygen vacancies in the ZnO created by the Al_2O_3. This discovery suggests a new route for realizing high performance memristor devices using 2D oxide heterostructures.

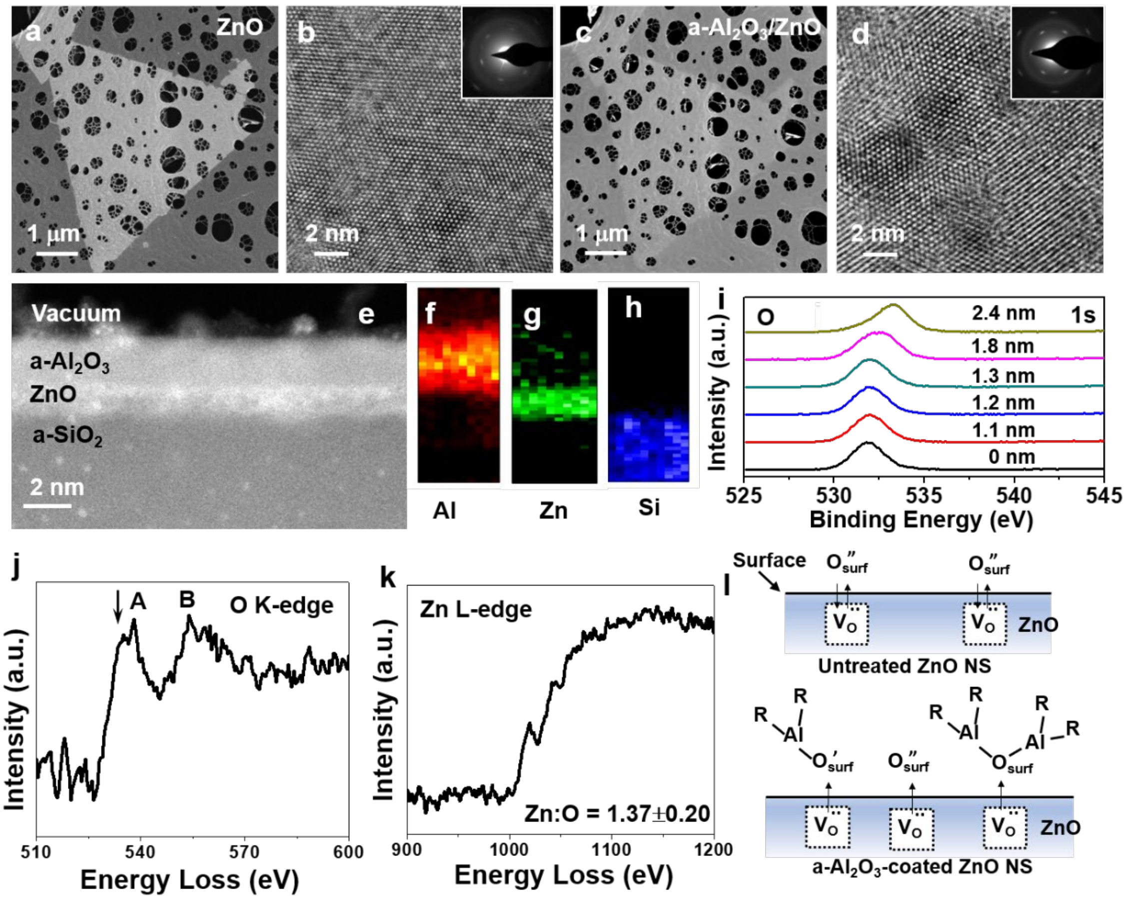

Figure. 16 Crystal structure characterization of ZnO and ZnO/Al_2O_3 nanosheets. (a) Low-magnification STEM image of one ZnO nanosheet resting on a TEM grid. (b) High-resolution TEM image showing the crystal lattice of wurtzite ZnO, viewed on the [0001] zone axis. Inset is the selected area electron diffraction (SAED) pattern confirming the single-crystalline wurtzite structure. (c) Low-magnification STEM image of one ZnO nanosheet coated by an amorphous Al_2O_3 layer on a TEM grid. (d) High-resolution TEM image showing of the wurtzite crystal lattice of ZnO nanosheet, indicating the ZnO nanosheet was not impaired by the Al_2O_3 deposition.

Inset is the SAED pattern. (e) Cross-section STEM image of one memristor device showing the stacking of the ZnO nanosheet and the amorphous Al_2O_3. The corresponding element mapping of (f) Al, (g) Zn, and (h) Si showing that each layer had a distinct area and there was no observable interaction among them. (i) Depth-profiling X-ray photoelectron spectroscopy of one memristor device, showing the oxygen peak shifted from 531.9 eV in Al_2O_3 to 532.4 eV in ZnO, and to 533.3 in SiO_2. Electron energy loss spectroscopy on cross section samples comparing the (j) O K-edge and (k) Zn L-edge from amorphous Al_2O_3 coated ZnO nanosheets. (l) The proposed mechanism for the evolution of high-concentration oxygen vacancies as a result of Al_2O_3 ALD.

8. Enhanced Ferromagnetism from Organic−Cerium Oxide Hybrid Ultrathin Nanosheets

2D organic−inorganic hybrid nanomaterials, such as 2D metal−organic frameworks and 2D organic−inorganic hybrid perovskites, were created as a new member of the 2D nanomaterial family, enabling unique property coupling. capping metal oxide with organic molecules could induce ferromagnetism by changing the electronic configuration through electron transfer between organic molecules and metal oxides. By using ILE, ultrathin cerium oxide nanosheets hybridized with stearic acid (SA) and oleylamine (OAM) molecules was synthesized. A significantly enhanced room-temperature ferromagnetism was recorded when the nanosheet thickness was reduced to 0.67 nm. The saturation magnetization was almost 5 times higher than that of CeO_2 thin films and more than 20 times higher than those of CeO_2 nanoparticles. The magnetization was attributed to the hybridization of organic surfactants with the CeO_{2-x} nanosheets, which stabilized the high concentration of Vo and induced electron transfer between the organic surfactant layer and cerium oxide layer.

The CeO_{2-x} nanosheets were synthesized at the water−air interface by ILE under a monolayer of mixed surfactants of SA and OAM at a ratio of 9:1 All of the nanosheets had a hexagonal shape, while their size exhibited a bimodal distribution: large ones had a diagonal length of 11.5 ± 0.8 μm and small ones were 2.3 ± 0.3 μm. Atomic force microscopy (AFM) topography image in revealed that the nanosheets had a very uniform thickness of 0.67 nm (Figure 17) with a surface roughness of only 0.13 nm. The thickness of hy-CeO_{2-x} nanosheets could be controlled by the precursor concentration. As the concentration of $Ce(NO_3)_3$ increased from 0.2 to 1 mM and 1.5 mM, the thickness was raised from 1.63 to 3.01 nm and 4.92 nm, respectively. XPS analysis of the as synthesized hy-CeO_{2-x} nanosheets revealed the coexistence of both Ce^{4+} and Ce^{3+}. Two peaks at 284.8 and 289.0 eV were observed in the C 1s region of all three-thickness nanosheets, and they could be assigned to the alkyl chain (C−C) and carboxylate (COO^-) carbon atoms, respectively, evidencing the presence of SA surfactants. A single peak at 399.7 eV corresponding to N 1s confirmed the presence of OAM on the nanosheet surface.

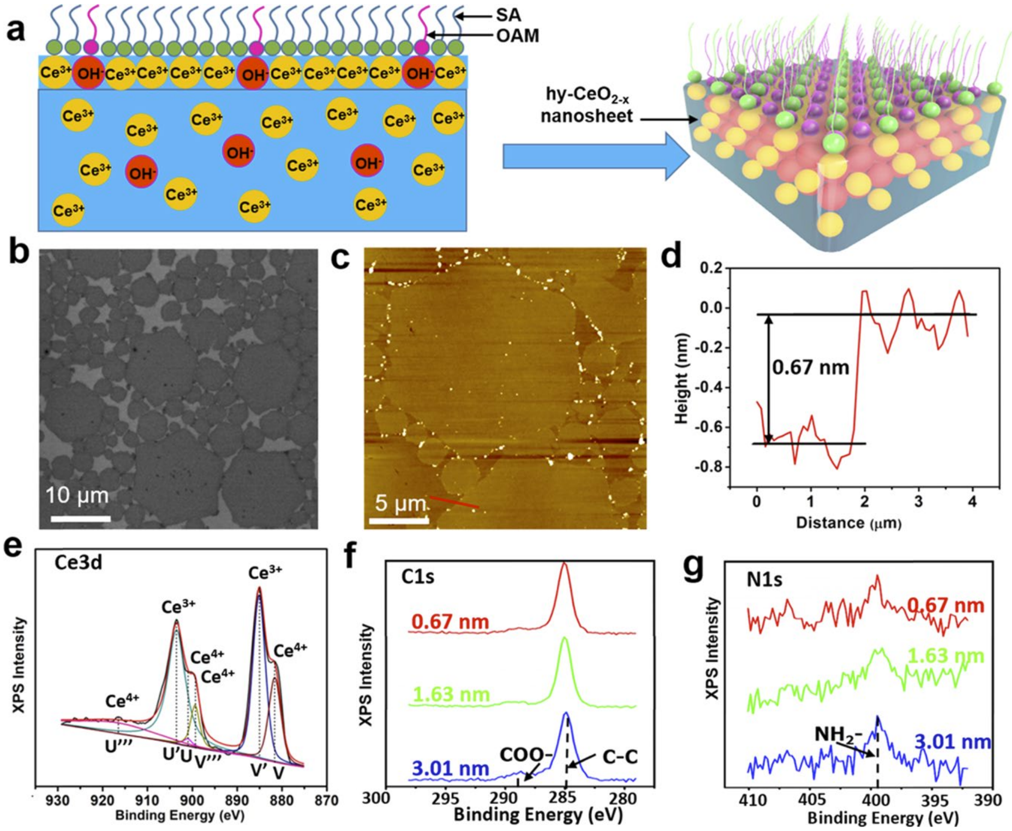

Figure 17. Synthesis, morphology, and elemental information of hy-CeO$_{2-x}$ nanosheets. (a) Schematic of ILE synthesis of hy-CeO$_{2-x}$ nanosheets. (b) SEM image of as-grown hy-CeO$_{2-x}$ nanosheets on a silicon substrate. (c) AFM topography scan of hy-CeO$_{2-x}$ nanosheets showing a uniform thickness. (d) Height profiles derived from the red line in (c). (e) XPS spectrum of characteristic X-ray peak of Ce 3d$_{3/2}$ and 3d$_{5/2}$ collected from the hy-CeO$_{2-x}$ nanosheets. (f) C 1s and (g) N 1s XPS spectra collected from the hy-CeO$_{2-x}$ nanosheets with thicknesses of 0.67, 1.63, and 3.01 nm.

The magnetic property of the as-synthesized hy-CeO$_{2-x}$ nanosheets with different thicknesses was examined by the magnetic hysteresis (M−H) loops measured at room temperature (Figure 18). As a comparison, results from CeO$_{2-x}$ nanoparticles synthesized under the same ILE condition were also included. They revealed that bare substrates had diamagnetic property and the ultrathin hy-CeO$_{2-x}$ nanosheets exhibited an obvious enhancement in ferromagnetic property as their thickness reduced from 3.01 to 0.67 nm. After subtracting the diamagnetic signals from the substrate, Figure 18a clearly shows that the hy-CeO$_{2-x}$ nanosheets with 3.01 nm thickness were paramagnetic. The1.63 nm hy-CeO$_{2-x}$ nanosheets showed ferromagnetism at low magnetic fields (−3000 to 3000 Oe), while paramagnetic contribution was still present at high magnetic fields. When the thickness was further reduced to 0.67 nm, the hy-CeO$_{2-x}$ nanosheets became completely ferromagnetic with a saturation magnetization (Ms) of 0.149 emu/g. The Ms of the ultrathinhy-CeO$_{2-x}$ nanosheets was almost 5 times larger than that of the reported CeO$_2$ thin films with a thickness of 40−50 nm, and 20 times larger than that of previously reported typical CeO$_2$ nanoparticles. Notably, CeO$_{2-x}$ nanoparticles synthesized under the same ILE conditions only exhibited diamagnetic property. M−H curves of the 1.63 and 0.67 nmhy-CeO$_{2-x}$ nanosheets measured at 5 K were compared to the room temperature results, as shown in Figure 18b. The magnetic behavior of 0.67 nm nanosheets was found nearly unchanged at 5 and 300 K. However, for the thicker 1.63 nm nanosheets, its saturation magnetization increased to 0.162 emu/g when the temperature reached 5 K.

High Vo concentration was found for all three-thickness samples. When a Vo is formed in CeO_2, two electrons are left behind and localized at the 4f orbital of the two neighboring Ce atoms. Thus, the valency of these two Ce atoms was reduced to +3. At a large Vo concentration, these Ce^{3+} ions can easily be re-oxidized to Ce^{4+} as the interaction between them would facilitate the removal of 4f electrons and thus makes Vo unstable. However, when organic molecules with negatively charged head groups are bonded to the surface, electrons transferred from the molecule could substitute the losing electrons and stabilize the Ce ions at +3. This could protect the neighboring Vo from being oxidized and thus stabilize the large concentration of Vo. Vo at the surface can induce nearly 50% higher magnetic moments than those induced by Vo in the bulk lattice. Despite having almost the same Vo concentration, the 0.67 nm-thick nanosheets had all of the ions and defects at the surface. The 1.63 and 3.01 nm thicknesses were corresponding to three and five unit cells, respectively, where more Vo could be distributed away from the surface. Therefore, the extremely higher surface-to-volume ratio resulted in a larger saturation magnetization in the 0.67 nm-thick hy-CeO_{2-x} nanosheets as compared to 1.63- and 3.01 nm-thick nanosheets. In addition, the organic surfactants layer can also induce ferromagnetism by electron transfer from the surfactant layer to the bonded Ce ions. Our work highlights the hybridization of the organic surfactant with the CeO_{2-x} nanosheets, which can enhance the magnetization of cerium oxide nanosheets. This strategy opens up a promising avenue toward exploring new physical properties of novel 2D organic− inorganic hybrid nanomaterials.

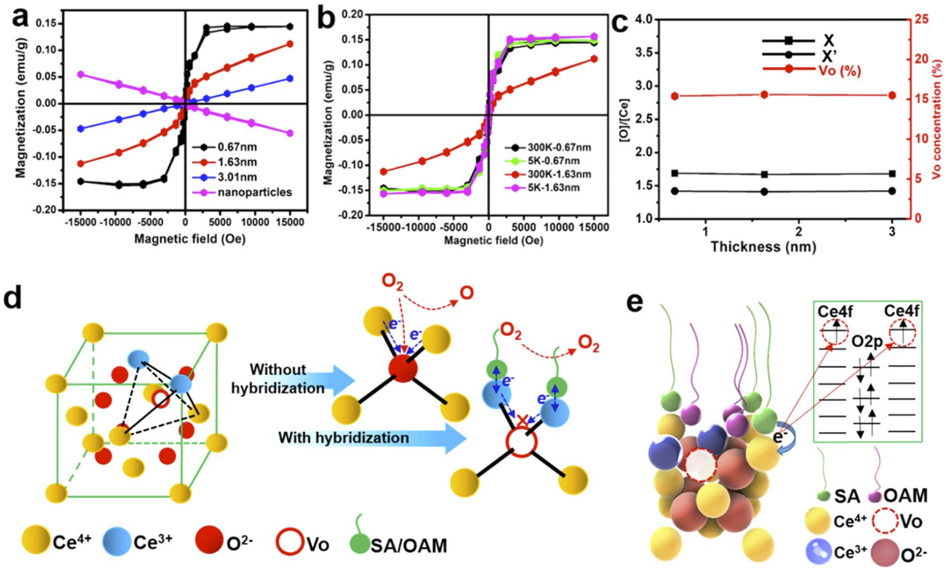

Figure 18. Magnetic properties of hy-CeO_{2-x} nanosheets. (a) M−H curves measured at 300 K from hy-CeO_{2-x} nanosheets with thicknesses of 0.67, 1.63, and 3.01 nm, respectively. The M−H curve from CeO_{2-x} nanoparticles is also shown for comparison. (b) Comparison of the M−H curves measured at 5 and 300 K for the 0.67 and 1.63 nm hy-CeO_{2-x} nanosheets. (c) CeO_{2-x} stoichiometry variations as a function of the nanosheet thickness calculated from the concentrations of Ce^{3+} and Ce^{4+} (black square), from the intensities of the O 1s and Ce 3d XPS peaks (black circle). Red hexagons represent the concentration of oxygen vacancy. (d) Schematic of how organic surfactant attachment would stabilize Vo in hy-CeO_{2-x}. (e) Schematic illustration of a single unit cell of hy-CeO_{2-x} nanosheets with an oxygen vacancy and how it contributes to magnetization.